such as the reduced tidal deformability, the stellar compactness or the maximum mass for a non-rotating NS, see e.g. [2337–2339, 3179, 3180].

Due to the variety of ejection processes and timescales, as well as to the anisotropic neutrino emission that characterizes merger remnants, the ejecta feature a broad range of electron fractions [3181, 3182]. The tidal ejecta are very neutron rich ($Y_e \sim 0.1$) and cold, while the shocked ejecta are reprocessed to higher Y_e by capture processes and neutrino irradiation from the NS remnant [2341, 3167]. The electron fraction in shocked ejecta can span a wide range of values, $Y_e \sim 0.1 - 0.4$, with the largest Y_e obtained at high latitudes where the neutrino fluxes are more intense. The inclusion of neutrino absorption has a direct impact on the r-process nucleosynthesis, as visible in the right panel of figure 135. The lifetime of a BNS merger remnant and, more in general, the presence of a massive NS or a BH in the center possibly affect the disk wind ejecta composition due to stronger or weaker neutrino irradiation [2355, 3183, 3184].

The observational imprint of r-process elements in compact binary mergers is the kilonova EM transient [3185–3187], see also section 5. The peak time and the spectral evolution of the light curves are influenced by the amount of the ejecta, as well as by its composition. In particular, if the r-process nucleosynthesis results in the synthesis of lanthanides or actinides, the resulting opacity is expected to increase by one or two orders of magnitudes, due to the opening of the electron f-shell [3188–3190]. The peak in the emission is then shifted toward later times and the spectrum becomes redder following the adiabatic cooling due to matter expansion. Kilonova modeling is extremely challenging, since it requires the solution of the photon radiative transfer problem in a fast expanding medium of ionized matter. The latter is composed by radioactive elements characterized by millions of atomic transitions whose strengths are poorly known. Moreover, the ejecta emerging from the collisions are characterized by a non-trivial geometry, due to the presence of different ejecta components, possibly characterized by a radial and angular dependence in the most relevant properties (mass distribution, expansion velocity, nucleosynthesis yields, etc), which are far from being isotropic or radially homogeneous, see e.g. [2341]. Sophisticated radiative transfer models have shown their ability in reproducing, at least at a qualitative level, the spectral features observed in AT2017gfo, e.g. [2181, 3191–3194]. They are mandatory to identify the presence of specific elements through distinct spectral features. A possible compromise for efficient line identification is represented by radiative transfer codes that model only the effects of the atmosphere on the photospheric emission, see e.g. [2257], while efficient kilonova models necessary for Bayesian analysis can rely on kilonova surrogate models of radiative transfert simulations [3195] or simplified semi-analytical solution of the radiative transfer equations [2343].

7.3.3.4 Multimessenger detections in compact binary mergers.

Gravitational waves and neutrinos. In the case of NS-BH or BNS mergers, a multimessenger detection possibly includes neutrinos and EM radiation, in addition to GWs. Thermal neutrino luminosities from BNS mergers were analyzed and compared with the corresponding GW luminosities [3196]. In the case of non-promptly collapsing remnants, both emissions seem to correlate with the mass-weighed tidal deformability $\tilde{\Lambda}$, eq. (7.5), with larger $\tilde{\Lambda}$ providing weaker luminosities. Both emissions show $\sim$1 kHz modulations associated to the violent radial bounces of the remnant's core, ultimately depending on the nuclear EOS properties. This kind of analysis would require a Galactic merger, which is extremely unlikely ($\sim 10^{-5}\mathrm{yr}^{-1}$). The detection of one event within the Local group ($\lesssim$ 3Mpc) could still results in $\mathcal{O}(10)$ neutrinos in future neutrino detectors. A more significant probability to observe thermal neutrinos in combination with GW signals from next-generation GW observatories will be realized only when megaton-scale ν detectors will be available. The impact of ET on these searches will be mostly limited to set triggers and alerts for well localized neutrino searches. However, the access to the post-merger signal, which is very likely in the case of nearby events, could better constrain the neutrino emission and the related nuclear physics, even by setting limits in the case of a lack of detections.

A more promising perspective is the multimessenger detection of GWs and non-thermal neutrinos. High-energy ($>$ TeV) non-thermal neutrinos are expected to be produced in gamma-ray bursts (GRBs) via photo-hadronic interactions between GRB photons and relativistic protons. During the prompt emission, these interactions lead to the production of pions, which decay into neutrinos. Additionally, during the extended emission phase, where the Lorentz factor of the jet becomes lower, the efficiency of meson production is enhanced, increasing the expected neutrino flux. For relatively nearby events ($< 100\,\mathrm{Mpc}$), the next-generation neutrino observatory, such as IceCube-gen2, will have the sensitivity required to detect neutrinos associated with ET detections of BNS or NSBH mergers [2369]. Another particularly interesting scenario occurs when a BNS merger results in the formation of a millisecond magnetar remnant surrounded by a low-mass ejecta shell. In this case, a fraction of the magnetar's rotational energy could be deposited in a pulsar wind nebula, accelerating ions to ultra-high energies. After $\sim \mathcal{O}(1)$ day, pion production in the resulting ion collisions could produce high-energy neutrinos. The resulting signal may be detectable in conjunction with GWs for individual mergers out to $\sim 100\,\mathrm{Mpc}$ by next-generation neutrino telescopes such as IceCube-Gen2 [2403]. Within such distances, ET could be able to detect the post-merger signal with a high enough signal-to-noise ratio to confirm the presence of a long-lived NS remnant and to set constraints on the nuclear EOS from the joint detection.

Gravitational waves and EM emission. The coincident detection of GWs and EM radiation has already disclosed its potential in constraining the nuclear EOS in the case of GW170817 and of its EM counterparts (GRB170817A and AT2017gfo). The reason is that the properties of the GW and EM emissions are influenced by nuclear physics in many different and often correlated ways, see, e.g., section 7.3 for the impact on the GW signal.

The contribution of ET to these multimessenger detections will be manifold, see section 5. First of all, ET will enlarge the detection horizon, and for longer signals, such as those from BNS mergers, ET will provide accurate sky localization even when operating as a single observatory. Section 5 demonstrates that the GW+kilonova detectable binaries are tens to a few hundreds per year by a telescope reaching an AB magnitude of around 26 in the g band and following up GW signals with a sky-localization smaller than $100\,\mathrm{deg}^2$. By exploring realistic observational strategies of ET operating with the Vera Rubin Observatory, ref. [2334] evaluates 10 to 100 detections per year and a detection increase of an order of magnitude when ET operates with Cosmic Explorer. The impact of the EOS of nuclear matter on the

GW+KN detection rate is found to be $\lesssim 20\%$ level for ET observing as a single detector and $\lesssim 40\%$ for the ET+CE network. While for kilonova emission, the horizon of joint detections is limited to $z \sim 0.5$, the larger horizon for GW+GRB detections will add tens to a few hundred joint GW+GRB detections per year (see section 5 and ref. [1175]). The resulting number of detections will be large enough to provide a significant exploration of the binary parameter space, probing different post-merger scenarios and the involved nuclear physics. The capability to localize compact binary merger events in the sky will allow deep and temporally extended follow-up campaigns, whose results will be detailed light curves and spectra from which the ejecta properties and composition could be accurately inferred (at least for the closer ones).

Second, ET will help break the degeneracies between the nuclear physics effects and the influence of the binary parameters on the post-merger dynamics and observables. In particular, for sufficiently nearby events, ET will allow a detailed GW parameter estimation to determine with high accuracy the properties of the merging objects and their tidal deformability, see section 7.3.1. In this way, the kilonova features and, if available, the post-merger GW signal can be more directly and firmly related to the post-merger dynamics and to the ejecta composition, and from that to the underlying nuclear physics. For example, post-merger models differing only in the high density and high temperature behavior of the EOS or featuring the appearance of hyperons or quarks (usually producing an EOS softening) could indeed be tested by their effects on the post-merger observables (for example, through their impact on the remnant lifetime or on the amount of ejected matter). In this respect, it is important to remark that the coincident detection of kilonova provides complementary information with respect to the GW signal alone since, even in the case of a long-lived remnant, the GW emission is expected to subside after a few tens of ms, while matter ejection and neutrino irradiation can last seconds and leave their fingerprints in the kilonova emission.

Third, in the case of a joint GW and kilonova detection, detailed modeling of the matter ejection and kilonova emission based on robust binary parameters extracted from the GW inspiral signal can provide constraints on the ejecta mass, on the nuclear heating rate and on the nucleosynthesis yields required to explain the observed light curves and spectra. However, starting from the same ejecta properties, different mass models can introduce up to a factor 10 of uncertainty in the kilonova brightness [3197, 3198]. It is thus clear that such a kind of analysis has the potential to determine the properties of the exotic nuclei involved in the r-process, see section 7.2.3.2.

Another relevant scenario for which next-generation GW observatories could be key is the one involving promptly collapsing BNS mergers. The latter have the potential of probing nuclear properties at the highest densities, especially if the threshold for prompt collapse is determined for different mass ratios, see, e.g., [3060] and 7.3.2.1. GW telescopes such as ET have the potential of directly probing the process of BH formation in promptly collapsing or short lived events [3199]. For the same events, the detection of the corresponding kilonova could discriminate between different mass ratios or different remnant lifetime: indeed, unequal mass mergers and short-lived remnant are expected to produce more ejecta and, thus, brighter kilonovae, while equal mass mergers tend to eject very small amount of ejecta [3057, 3166, 3178].

JCAP03(2026)081

The joint detection of GWs and of a short GRB signal (prompt or afterglow emission) has the potential of shading light on the nature of the central GRB engine. In particular, assuming that the post-merger signal could be detected up to ∼100 Mpc by ET, the expected joint detection rate involving a post-merger signal can be estimated to be $\sim 0.03 - 0.6\,\mathrm{yr}^{-1}$ [2336, 3200]. Such a detection could directly discriminate between the magnetar and the BH central engine scenarios for the production of a relativistic jet. Additionally, the precise localization of compact binary mergers allowed by ET can also favor the discovery of faint emissions from chocked jets. The precise knowledge of the central engine, combined with the measured rates of successful short GRBs and of merging binaries by GW observations, can provide independent constraints on the maximum NS mass and, from that, on the EOS of nuclear matter, see, e.g., [3007, 3201]. Recent detection of nearby ($z \lesssim 0.1$) long GRBs with kilonova-like signatures have questioned the long-standing paradigm of long-GRBs always originating from core collapses, see, e.g., [2252, 2303, 2306]. These observations points on the possibility for compact mergers to produce long GRBs. Since ET will be able to detect compact mergers up to an horizon of $z = 3-4$ [16], in the case of long GRB with kilonova-like signatures, it has the capability to firmly confirm this scenario.

7.3.3.5 Data analysis and modeling efforts. The rigorous analysis of multi-messenger signals requires a Bayesian approach. Constraints on the EOS of nuclear matter and on specific NS properties (for example, the maximum mass of a non-rotating NS or the radius of a 1.4 or 1.6 $M_\odot$ NS) were obtained by combining parameters extracted from the inspiral signal of GW170817 and GW190425, detailed models of the EM counterparts, additional astrophysical and nuclear physics constraints (e.g., maximum observed NS masses, NS radii as obtained by the NICER mission or data extracted from heavy-ion collisions) and non-trivial relations connecting the remnant and ejecta properties to the nuclear EOS (as obtained by detailed compact binary merger simulations), see, e.g., [2289, 2342, 2612, 2745, 3202–3209]. Even the non-detection of EM counterparts, if not due to insufficient accuracy in the sky localization or EM follow-up coverage, can provide constraints on the nuclear EOS, as in the case of GW190425, see, e.g., [3210–3212]. In the case of (i) large correlations between the parameters describing the different observations and (ii) systematics in the modeling, the analysis of different data coming from a single source benefits from a joint and coherent analyses. In this kind of analysis, single messenger likelihoods are joined and a combined sampling of the full posterior probability distribution is performed. This approach was recently implemented and presented in refs. [2461, 3213, 3214]. It allows joint and coherent analyses of multimessenger signals, including GWs, kilonovae/supernovae and GRBs, possibly taking into account quantitative relations inferred by large sets of sophisticated simulations connecting the source intrinsic properties (for example, the masses of two merging neutron stars) to the ejecta properties, nuclear-physics constraints at low densities and multiband observations of isolated NSs, as visible in figure 136.

It is thus clear that the full exploitation of future multimessenger observations involving GW detections from ET will rely on detailed and reliable models of the sources that contains detailed nuclear physics. This will require a great community effort within the next ten years. The ambitious goal will be to connect the strong field dynamics that characterizes the emission of GWs and neutrinos, as well as the expulsion of matter, to the resulting light

JCAP03(2026)081

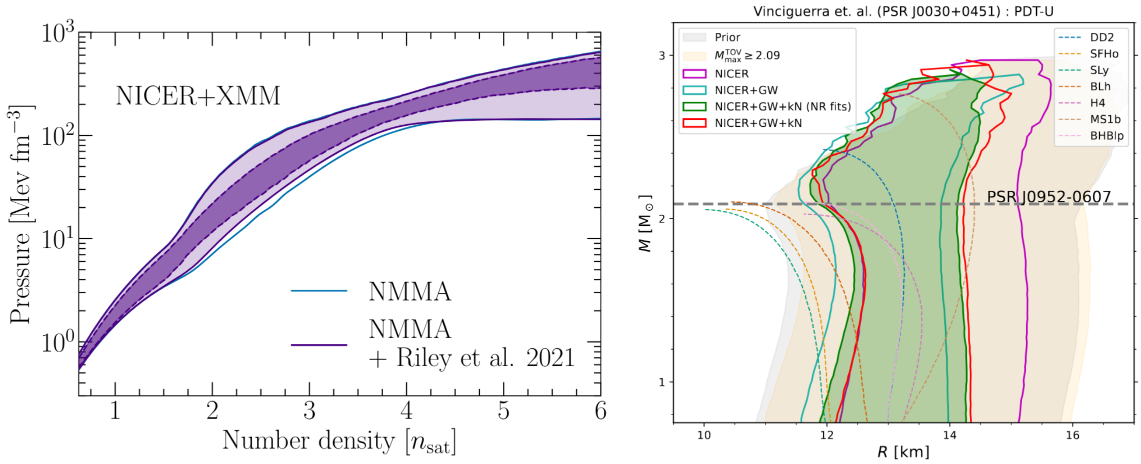

Figure 136. Examples of constraints on the nuclear EOS obtained by joint multimessenger analysis combining astrophysical observations of pulsars, NICER measurements, GW170817 and GW190425, kilonova AT2017gfo and GRB170817A modeling. *Left:* posteriors for the pressure as a function of number density with (purple) and without (blue) NICER and XMM observations of PSR J0740+6620. *Right:* posteriors in the M-R diagram of the GW-only (blue), joint (red), and NR-informed joint analysis (green). Figures reproduced from [3208]. © 2021. The American Astronomical Society. All rights reserved (left) and Reproduced from [3214]. CC BY 4.0 (right).

curves and spectral features that allow to quantify the amount of ejecta and its properties through the identification of elements. For standard CCSNe, three-dimensional, self-consistent exploding simulations, characterized by a high level of fidelity in the neutrino transport, are now available. Future models should also include consistent nucleosynthesis yields predictions and extend up to shock breakout. The inclusion of magneto-hydrodynamics effects in CCSN models to predict their imprint will also be key. In case of a sufficiently close-by CCSN, jet-like features in the GW, neutrino and electromagnetic signals can be a smoking gun for the viability of magneto-rotationally driven SNe. Reliable collapsar simulations, addressing both the formation of the relativistic jet and the nucleosynthesis of the innermost ejecta, will be also necessary to probe the central engine of gamma-ray burst related to SNe. In the case of compact binary mergers, the ambitious goal will be the production of reliable end-to-end models, i.e., models that seamlessly connect the GW inspiral signal to the emission of EM radiation that characterizes the gamma-ray burst and the kilonova, as well as their afterglows [2259, 3215, 3216]. Open challenges here are represented by the inclusion of detailed neutrino transport and microphysics in merger models (see also section 7.4.2), the modeling of the central engine producing the relativistic jet, as well as its interaction with the surrounding medium. In terms of kilonova emission, large effort will be devoted to the calculation of opacities and spectral features that can unambiguously identify the presence and the amount of specific elements in the ejecta.

A great challenge ahead is also represented by the inclusion of neutrino oscillations in models of CCSNe and compact binary mergers. While the effect of vacuum and matter oscillations is presently accounted for the determination of the expected neutrino signal, the role of neutrino-induced oscillations, their impact on the remnant dynamics and on the nucleosynthesis are possibly significant, but still under investigation, see, e.g., [3217–3221].

7.4 Uncertainties and degeneracies in our measurements

To properly extract the information from GW observations, one has to cross-correlate the observational data to theoretical models. In this section, we discuss the impact that various uncertainties in GW modeling and theoretical assumptions may have on the interpretation of ET data for subatomic physics. For a detailed discussion about waveform modeling, we refer to section 9.

7.4.1 Impact of waveform-model uncertainties

7.4.1.1 Inspiral-merger. During the inspiral, characteristic matter signatures in the GW signal arise primarily due to spin and tidal effects, including dynamical tides associated with the excitation of the star's internal oscillation modes, and, in NS-BH systems, also the possible tidal disruption of the NS. Waveforms describing the inspiral of compact binaries with at least one NS are commonly built by augmenting a high-fidelity point-mass, i.e., binary BH (BBH), baseline with matter-induced corrections. A more detailed overview of the current state-of-the art waveform models for BNS and BHNS can be found in section 9.

Spin effects that depend on the EOS first enter the GWs through the spin-induced quadrupole moment with the same scaling in frequency as post-2-Newtonian (2PN) point-mass effects. For tidal effects, the dominant adiabatic (static) contribution first enters the GW phase with a scaling in frequency similar to a 5PN term [3222] and higher order corrections to these effects are currently known to relative 2.5PN order [3223, 3224], while non-spinning point-mass effects are currently known completely up to 4PN order. More recently, calculations within the effective-one-body framework as well as PN theory have been carried out to start incorporating dynamical tidal effects from the f-modes into BNS waveform models [2881, 3225–3229]. Even though these effects are most prominent at a GW frequency of around 800 Hz, they accumulate over a wide range of frequencies and, for a detector like ET, neglecting these effects can lead to systematic biases in the inferred NS radius by more than 1 km [3230–3232], i.e., they have to be incorporated to achieve the estimated accuracies discussed in section 7.3.1.1, which only account for statistical uncertainties. In addition, other NS modes such as r-modes and g-modes can become resonantly excited much earlier in the inspiral and accumulate significant information, see e.g. [2882, 2917, 3233–3238] for recent work and further references. Moreover, nonlinear tides may also play a non-negligible role [3239]. Spins further affect tidal phenomena, e.g., they lead to effective shifts in the resonance frequencies [2880, 3240] and new interactions characterized by spin-tidal Love numbers [3241, 3242]. Other physics may also play a role, e.g., the NS viscosity [2894, 3243]; see section 7.2.3.1, and a nonnegligible temperature induced by mode excitations as estimated in [2886]; see section 7.3.2.1. However, such consequences remain to be explored in more realistic settings. Additionally, the effects of eccentricity could alter the dynamics, in turn impacting tidal effects [3244, 3245] and thus influencing the inference of EOS physics, as remains to be quantified. In summary, incomplete knowledge of the point-mass baseline model and more realistic physical effects can have a significant impact on the measurement of tidal parameters. The implications for ET remain to be comprehensively analyzed once theoretical models are further developed. The main theoretical tools to understand and model the currently missing effects are in hand, but further work is needed to determine which phenomena are essential for the majority of NS binary signals when incorporating more realistic physics.

Currently, shortcomings in the analytical knowledge of the point-mass baseline are reduced by including phenomenological corrections to incorporate non-perturbative information from NR simulations and in some cases also more theoretical knowledge from other channels such as gravitational self-force. Importantly, while the current BBH baseline models such as `IMRPhenomXPHM` [3246, 3247] and `SEOBNRv5PHM` [3248, 3249] are found to be sufficiently accurate across a large part of the parameter space for current-generation GW detectors, systematic differences due to modeling choices are already becoming apparent in more challenging parts of the parameter space, e.g. [3250]. Shortcomings in these baselines impact the inference of all source parameters and hence the EOS reconstruction from global NS properties, including the masses. Moreover, current models that include matter effects (e.g. `NRTidalv3` [3229], `SEOBNRv4T` [3225, 3226], `TEOBResumS` [3251]; see section 9 for details on these models) remain even more limited than those for BBHs in both the parameter space covered and the additional physics included, such as the magnitude of spins, spin precession effects due to the misalignment between the component spins and the orbital angular momentum, orbital eccentricity, and higher modes. Spin-precession effects have been shown to be essential to avoid biases in the measurement of the source masses [1864, 3252], which in turn impacts the inference of the mass-radius relationship, and higher-order modes will be especially important for NS-BH systems due to the larger mass ratio of these class of objects. Any such shortcoming further impacts the measurements of tidal parameters. The extent of these impacts remains to be quantified, however, existing estimates already indicate the need for advances in modeling to include such effects.

To capture the tidal imprints in the waveform phasing during the late stages of the inspiral, phenomenological expressions informed by NR simulations have been developed. However, their tuning is limited in mass ratio, spin magnitude, and orientation, as well as the dominant quadrupolar mode and BNS systems. Recent progress has been made by extending the calibration range to more asymmetric binaries and incorporating more analytical information into the structure of the model, e.g., [3229]. However, ET will be sensitive to even more subtle matter effects, as discussed above, that could alter the morphology of the signal and have not yet been included in such state-of-the-art models.

An additional tidal signature that occurs in NS-BH binaries is the complete or partial disruption of the NS, which also gives rise to an electromagnetic counterpart. While disruption preferentially occurs for binaries with similar masses, large BH spins and stiffer EOS, the recent observation of GW230529 [1475] suggests that such events may be more common than previously expected. Currently, tidal disruption is only treated phenomenologically and modelled as a sudden dropoff in the waveform amplitude [3253–3255]. The disruption frequency and its main parameter dependencies have been explored in full NR simulations, which are challenging to carry out, as explained in detail in section 9, and have been limited in their parameter space coverage. Under the assumption of a perfect model, the improved

JCAP03(2026)081

detector sensitivity alone will allow us to determine the disruption frequency within $\sim 100\,\mathrm{Hz}$, which translates into an NS radius measurement accuracy of ~ 1 km [3256], with much tighter constraints possible when combining this with the information on tidal deformability from the inspiral phasing.

7.4.1.2 Post-Merge. Due to the complex multi-scale physics involved, the modeling of the post-merger GW emission is very challenging and involves extreme densities, temperatures, and magnetic field strengths. We also note that, as discussed in section 7.3.2.1, only a fraction of BNS mergers are expected to exhibit such rich post-merger behavior, while others will promptly collapse to a BH. Understanding and modeling the post-merger phase of the binary evolution requires NR simulations. However, NR simulations are limited by uncertainties from numerical inaccuracies (which increase in the presence of shocks) and incomplete descriptions of the microscopic physics. Given the high temperatures and densities after the merger and the possibility of increased magnetic field strength by orders of magnitude during the merger, the physical inputs, which are of interest when constraining the EOS, alter the postmerger GW signal noticeably more than during the inspiral. For example, the emission of neutrinos reduces the remnant's temperature and leads to an earlier BH formation. Similarly, a possible quark-hadron phase transition (that might appear in the post-merger phase) might noticeably change the compactness of the remnant and, therefore, shift the emission frequency of the post-merger GW signal, e.g., [2471, 3011, 3257]. All of these influences must be quantified to extract information from the postmerger GW signal reliably; see section 7.4.2.

Up to now, there have been several attempts to construct postmerger models, e.g., [2464, 2467, 3014–3019, 3063, 3258], by capturing the most important characteristic frequencies from the postmerger remnant. While our understanding of the main emission frequencies continuously increases, existing estimates still have uncertainties of about 100 Hz. These differences are of the same order as differences in the postmerger spectra due to interesting physical processes; for example, it has been outlined [3259] that pion production could lead to a frequency shift of about 150 Hz. To further improve our understanding of the postmerger spectrum, one would need a larger set of NR simulations with well-quantified error bars across a large range of the BNS parameter space and with accurate modeling of microphysical processes. Given the enormous complexity of physics and scales involved, and despite recent progress on novel codes (e.g. [3260]), it is likely that computing thousands of NR waveforms with sufficient resolution, physical realism, and parameter space coverage to build accurate waveforms (e.g. via surrogates) for parameter inference of BNS mergers will remain out of reach for the next decade.

However, it is possible to instead adopt a data-driven approach, for instance, by using a morphology-independent method to reconstruct the postmerger GW signal [3020, 3026]. Such analysis strategies have the advantage that information of the GW spectrum can be directly extracted without reliance on models. However, the interpretation of these results for the underlying source physics still requires theoretical models.

Irrespective of the data analysis approach, extracting the main emission frequencies from the postmerger remnant will remain challenging even with ET and will only be possible for BNS sources with a minimum postmerger signal-to-noise ratio of about ~ 5 [3016]. Depending on the properties of the source, this corresponds to distances of less than 100 Mpc. Hence, only a few of the closest BNS systems will provide reliable information on postmerger physics. For these sources, the properties of the progenitors would be measured by ET with high accuracy from the inspiral physics, which will aid in the analysis of the postmerger signals.

7.4.2 Uncertainties in simulations and microphysics input

Due to the complexity of Einstein's field equations, NR simulations are an essential tool to improve our understanding of the merging of BNS and NS-BH systems [3008, 3261, 3262]. However, despite continuous progress and simulations with increasing accuracy, e.g., [3263–3269], these simulations have different sources of errors and uncertainties which have to be taken into account when using numerical-relativity simulations to extract information from future observations of NS mergers. Uncertainties in such simulations arise, on the one hand, due to numerical approximation when solving the GR field equations together with those of general relativistic hydrodynamics and on the other, due to the incorporation of microphysical processes, such as neutrino and photon radiation, magnetic-field amplification, or viscous effects. In the following, we briefly discuss the dominant sources of uncertainty.

7.4.2.1 Numerical Discretization. In contrast to the simulation of black-hole spacetimes, simulations of supernova explosions or compact binaries including at least one NS, not only need to find an accurate description for the simulation of the spacetime but also have to deal with general-relativistic hydrodynamics. This adds to the complexity that at the surface of the NS, the shocks and discontinuities have to be described properly. Until now, most numerical codes used for such simulations use either finite differencing or spectral methods for the spacetime, and high-resolution shock-capturing schemes based on finite differencing or finite-volume methods for the hydrodynamical equations. Irrespective of the numerical methods employed, the discretization typically introduces an error that has to be carefully checked by computing numerous resolutions. In the past, several groups have assessed the uncertainty of their simulations and found errors in the phase of the extracted gravitational-wave signal of about $\mathcal{O}(0.1)$ rad up to $\mathcal{O}(1)$ rad accumulated over the last 10 to 20 orbits before the merger [3263, 3266, 3268–3271]. This typically leads to mismatches that are larger than the target accuracy required for ET. However, recent progress has also been made on using discontinous-Galerkin methods [3272, 3273] and developing exascale computing codes that will be a promising tool in the upcoming years, e.g., [3274]. In addition, alternatives to the ordinary high-resolution shock-capturing schemes and Riemann solvers have been proposed to reduce the uncertainty without increasing the computational footprint of the simulations [3269, 3275]. Overall, it will be crucial to explore alternative techniques to ensure efficient use of the computational hardware. Without such significant progress, based on the accuracy improvements obtained over the last decade, e.g., [3268, 3276, 3277], the accuracy targets will not be reached, which — as discussed in section 9 — will limit the development of improved GW models.

Moreover, uncertainties related to the finite volume of the simulation domain, though typically smaller than discretization errors, might also impact ET science. Most notably, the finite domain size leads to an extraction of the GW at a finite distance from the emitting system. At these distances, the linear approximation typically employed to describe GWs might not fully apply, and additional errors are introduced. Polynomial extrapolation employing different extraction radii or next-to-leading order information about the GW falloff behavior can improve on this, e.g., [3266]. While increasing the accuracy of the simulation and the extracted GW, this increased accuracy will likely still be too low. Hence, one has to expect that all future simulations aiming to produce accurate simulations for developing new waveform models employed in the ET era will have to use Cauchy Characteristic Extraction [3278], a method that ensures that GWs propagate to future null infinity where they can be properly and accurately extracted.

7.4.2.2 Matter-composition and simulating neutrino radiation. In addition to the uncertainty introduced by numerical discretization, our limited knowledge about the input physics is causing uncertainties in NR simulations. Among the most important unknown effects are composition effects of the EOS describing the material inside the NSs. Certainly, an understanding of the EOS and composition is among the science drivers for ET, and hence, one can not assume to have complete knowledge about these aspects. However, this might cause substantial problems, e.g., there have been numerous studies in the field outlining the existence of quasi-universal relations connecting postmerger properties to the binary properties, see section 7.3.2.1, but these relations might break in the presence of a strong phase transition, e.g., [2471, 3011]. Furthermore, the influence of pions or muons on the merger dynamics has also not been understood in detail [3279, 3280], and the role of viscous or out-of-equilibrium effects have to be quantified in greater depth, e.g., [2458, 3038]. Clearly, such studies are of interest to be prepared for upcoming ET discoveries so that observational data can be correctly interpreted, and the community has recently started to make increasing progress in this direction — see section 7.2 and section 7.3.1.1 for more detailed discussions.

Another issue regarding the correct simulation of the composition is the inclusion of neutrino interactions. The correct approach for including neutrinos in NR simulations would require solving equations for relativistic neutrino transport. However, these equations, coupled with the equations of general relativity and general relativistic hydrodynamics, are computationally too expensive to be solved directly. The reason is that, in addition to three spatial and one-time dimensions, three dimensions in the neutrino momentum space would need to be resolved. This 3+3+1-dimensional parameter space is too large considering the existing (and likely also upcoming) high-performance computing facilities. Hence, the community is still focusing on finding good approximations of the relativistic Boltzmann Equations; see [3281] for a recent review.

7.4.2.3 Simulating Magnetic fields. Another possible accuracy limitation of current simulations is the treatment of magnetic fields. While studies such as the results shown in figure 137, where the upper (lower) panel corresponds to a system without (with) magnetic fields, have shown that, for most scenarios, the magnetic field strength is insufficient to cause a large difference during the inspiral dynamics, the postmerger evolution will be affected by the magnetic fields. This is due to magnetic field amplification during the merger through the Kelvin-Helmholtz or the magnetorotational instability [3283–3288]. After merger, magnetized winds and jetted outflows can be launched by the now dynamically relevant magnetic field for both black hole and NS remnants [3289–3291]. This has a direct impact on the electromagnetic counterparts signals expected from these events, see section 7.3.3. A challenge in current

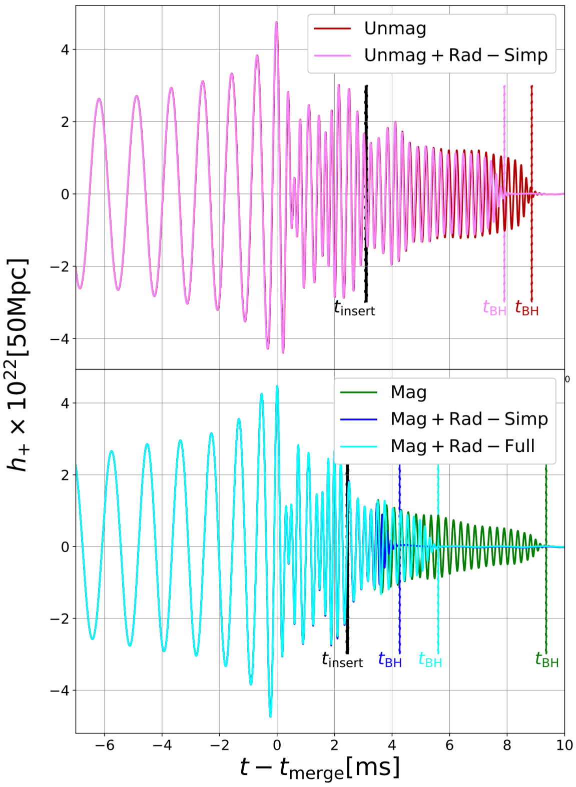

Figure 137. Influence of magnetic field and neutrino emission in the post-merger phase of a specific BNS simulation. Vertical lines mark the neutrino insertion (Mag + Rad cases), and BH formation. Reprinted figure with permission from [3282], Copyright (2022) by the American Physical Society.

state-of-the-art general-relativistic magnetohydrodynamics simulations of NS mergers is to resolve the turbulent magnetic field amplification and the resulting nonlinear small- and large-scale dynamo processes. High-resolution simulations showed that the length scales driving small-scale dynamos in the early merger are clearly unresolved [3044, 3047] and at least two orders of magnitude below the currently highest resolution simulations available but that resolving the magnetorotational instability in the later postmerger evolution can lead to large-scale magnetic field generation [3177]. Alternative approaches to incorporate the unresolved merger and early post-merger sub-grid scale effects are underway, e.g., general-relativistic large-eddy simulation schemes, e.g., [3034, 3292–3295]. However, such approaches are challenging, and most of the proposed methods are coordinate-dependent and do not provide a covariant formulation; see [3296] for recent progress. Hence, further developmental work on both the theoretical and computational side is needed to ensure that magnetic fields are properly modelled, which requires a better description of turbulent flow and small-scale effects. Additionally, beyond-ideal general relativistic magnetohydrodynamics (GRMHD) effects play a key role in how particles are accelerated in jetted outflows from BNS remnants. Hence, such effects have to be modeled to systematically connect GRMHD BNS simulations to their potential short-GRB signatures. While there are a small number of resistive GRMHD simulations [3297, 3298], more work is needed to develop resistive GRMHD simulation

JCAP03(2026)081

capabilities with all the necessary nuclear and neutrino physics included. Effects from the nuclear stress-energy tensor, such as bulk viscosity, may also play an important role and have only just begun to be included. This is partly due to the complexity of finding suitable and stable formulations of the viscous GRMHD equations that are numerically feasible, e.g., [3299]. Including all of these beyond-ideal effects will require significant development efforts from the community.

7.4.3 Degeneracies with modified gravity and Beyond-Standard-Model physics

Determining the EOS from GW data requires assuming an underlying theory of gravity. Even though most of the existent analyses assume General Relativity (GR), one can plausibly argue that its modification might be necessary and convenient in cosmology or help in building a consistent quantum-gravity theory (see section 2 for further detail). Section 7.4.3.1 addresses the influence of modified gravity on the structure of NSs and possible degeneracies with effects coming from the EOS uncertainties [3300]. Even if GR is adopted, other new physical effects, e.g., from the presence of dark matter, could impact the inference of the subatomic EOS from measurements. Such effects of Beyond the Standard Model (BSM) non-QCD matter are discussed in sections 7.4.3.2 and 7.4.3.3. We note that much of the material discussed in this section is an active and relatively new area of research. Consequently, the examples discussed below mainly serve to illustrate possible phenomena that have been uncovered and point out potential degeneracies with changes in the EOS in qualitative terms, while detailed studies of such degeneracies and implications for data analysis strategies remain an open problem.

7.4.3.1 Degeneracy of EOS uncertainties with gravity beyond GR. The degeneracies between EOS uncertainties and gravity beyond GR are far-reaching, covering both the equilibrium properties of NSs as well as their dynamics. Perhaps the best-known example is the degeneracy in the mass-radius diagram. This is demonstrated in figure 138 (left panel), which represents $M(R)$ dependencies for two EOSs within GR and for higher-curvature theories of gravity where one substitutes $R \to f(R)$ in the gravitational action, with the choice $f(R) = R + \alpha R^2$ [3301] and α a parameter.[64] For example, a hypothetical simultaneous measurement of the mass and radius of a NS as indicated by a grey dot might signal either that the true EOS is SLy or that we actually have a GR modification and the correct EOS is APR4. Such degeneracies are very common, and they reduce our ability to disentangle the two effects. Hence, extracting an EOS from the $M(R)$ diagram alone, which is in one-to-one correspondence in GR, becomes extremely difficult if alternative theories of gravity are considered.

Another example is represented in the right panel of figure 138. The mass-radius diagram shows how a typical EOS (dashed green line [2613]) is modified by (a) adding a first-order phase transition, visible as a kink, at around $R = 13\,\text{km}$ in the black-dashed line, or (b) using the modified-gravity Palatini $R + \alpha R^2$ [406] TOV equations with a parameter $\alpha = 150$ (solid green line). The two modifications would be practically indistinguishable over most of the range without extremely precise data (two data bars are shown to understand current

[64]We stress that the choice of a particular theory beyond GR, and the values of its parameters, are chosen mainly for illustrative purposes and better visualization.

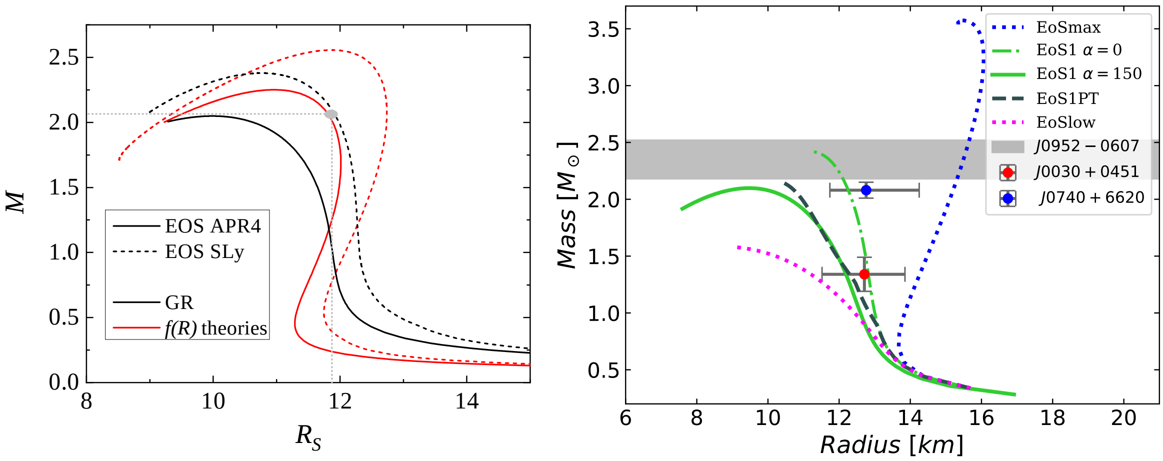

Figure 138. *Left:* the $M(R)$ curve for two EOS and two theories of gravity — GR and metric $f(R) = R + \alpha R^2$ gravity. Reproduced from [3302]. Published under licence by IOP Publishing Ltd. All rights reserved. *Right:* $M(R)$ curves from a typical EOS (green dashed line) modified by either a phase transition (black dashed line) or Palatini $f(R)$ gravity (solid green line). Superposed are example current and near-term pulsar measurement uncertainties [1819, 3303, 3304]. Reproduced from [406]. © 2024 IOP Publishing Ltd and Sissa Medialab. All rights reserved.

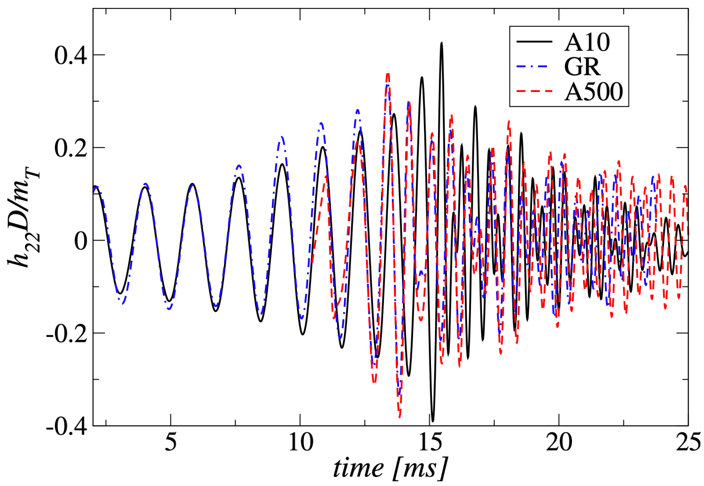

Figure 139. Influence of different values of the coupling constant α of $f(R) = R + \alpha R^2$ gravity on the post-merger GW signal (A10 computed with $\alpha = 21.8\,\mathrm{km}^2$, A500 with $\alpha = 1090.3\,\mathrm{km}^2$). (Time shifted so that the peak strain is simultaneous to that in GR). Reprinted figure with permission from [3305], Copyright (2018) by the American Physical Society.

precision in this diagram). It is interesting that such complicated phenomena like kinks, i.e. nonanalyticities, points of discontinuous derivatives in the EOS due to the latent heat of the phase transition [3306] in subatomic matter, can be mimicked by modified gravity. Another interesting example of a non-trivial degeneracy is the phase transition between two equilibrium states of NSs caused by the formation or the complete dissolution of a scalar condensate above a certain threshold condition [3307, 3308]. This process shares many similarities with a potential first-order phase transition between normal nuclear matter and

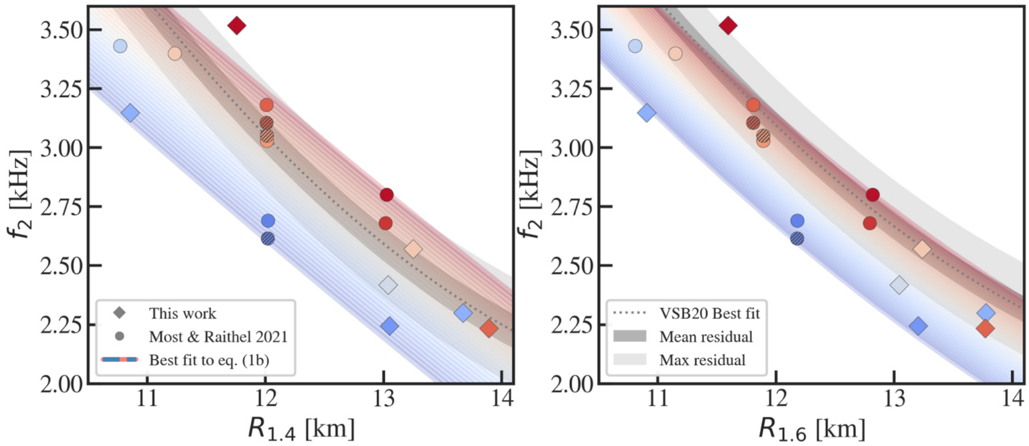

Figure 140. The universal relation for the peak frequency of the remainder following a neutron-star binary merger breaks down even in GR if the band of EOS used is broad enough: full tests of the gravity theory will need good control of the EOS from other sources. Reproduced from [3309]. The Author(s). CC BY 4.0.

deconfined quark matter in the stellar cores. As discussed in subsection 7.3.1.1, ET has the potential to determine NS radii down to 0.1 km. Even falling short of that goal would be extremely useful in this diagram, given that current uncertainties are over $\times 10$ times larger [2460]. We refer to [402] for the equivalent tidal deformability vs. mass diagram, which is the quantity directly relevant for GW measurements, while the radius is only inferred from the resulting preferred EOSs.

In addition to modifying properties of individual NSs and their binary inspirals, the theory of gravity also impacts the postmerger phase, as shown for the strain in figure 139. A popular method to test the theory of gravity without having to worry about the underlying EOS is the use of universal relations [409, 3310, 3311] that correlate quantities, like the dominant frequency following a binary merger and the radius of a cold spherically symmetric NS in β-equilibrium. These relations generally no longer hold in theories beyond GR. However, even within GR, such relations tend to be empirical and based on computing with a swath of EOS, whereas they sometimes fail when checked with a broader choice of EOS (colored symbols in the example of figure 140, that are out of the initially predicted grey band). Hence, a violation of quasi-universal relations could hint at multiple things: (i) interesting nuclear physics such as phase transitions, (ii) modifications of GR, (iii) too uncertain NR simulations employed to derive the quasi-universal relations, or (iv) a non ideal choice of variables for the quasi-universal relation. The latter is actually the case for the example shown in figure 140, where a rescaling of the frequency and the radius with the NS mass leads to much tighter and better fulfilled relations for a large set of NR data [3019].

Moreover, similarly to the case of a BNS merger, a close (within 10 kiloparsecs) supernova event's f-mode is expected to be reconstructible by ET with 90% accuracy [3312] in the frequency measurement. While we should be able to extract information about the EOS from it, once again, modifications to GR can produce degeneracies as outlined in ref. [3313].

Despite the mentioned matter-gravity degeneracies, interesting features in modified gravity can sometimes be solely attributed to the generalization of Einstein's equations. One such example is the existence of additional polarizations of the gravitational waves not present in GR, such as a scalar "breathing mode", a scalar longitudinal mode, and any vector modes [2486]. Special attention has been paid to the "breathing mode", present in certain classes of scalar-tensor models (such as Brans-Dicke theory). It can lead to interesting scalar-field induced GW signals, potentially detectable with ET [204, 3307, 3314].

7.4.3.2 Dark matter and other BSM physics. Models of the galactic dark matter (DM) halo (e.g. [3315]) suggest that many NSs may not be in vacuum but rather in a DM environment. As a consequence, NSs could accumulate a nonnegligible amount of DM within their interiors and vicinity, depending on the nature of the DM. Studies of the capture cross-section for DM particles such as [3316] imply that it is possible that NSs could efficiently thermalize and accumulate enough DM to affect their macroscopic astrophysical properties.

Depending on its nature, quantum numbers, and particles' mass, the effects of DM on the NS include modification of mass, radius, tidal deformability, kinematic properties, thermal evolution, x-ray pulse profile, etc [3317–3320]. As the nature of DM is unknown, proposed model DM particles span a broad mass range, from ultralight ($< 1\,\mathrm{keV}$) to heavy ($\gtrsim \mathrm{GeV}$) [3321]. Here, selected DM candidates and their impact on compact stars are briefly discussed, and we refer to section 2 for more details.

An observable of special note is the NS cooling behavior [3322], where DM can lead to a higher temperature plateau for old NSs. Such indications of a nonvanishing DM fraction in some NSs is complementary to signatures of matter properties in the GW signal [3323]. Recent work [3324] has also considered the efficiency of scalar-vector field theories describing the DM sector to reproduce current astrophysical measurements. In this way it is possible to further constrain the available DM parameter space complementarily to other existing bounds.

The impacts of DM on NS structure depend on the DM properties. Very weakly interacting dust-like DM acts by increasing the net energy density of the star without increasing the pressure, and thus at a given mass, the star contracts and the tidal deformability drops as R^5. The effect of such DM is akin to a softening of the EOS. Moreover, the presence of DM has been found to be potentially capable of triggering a phase transition to a quark star [3325]. This arises because the added DM increases the compactness of the NS at a given mass, which could make it energetically favorable to change at least part of the subatomic matter to a non-nucleonic phase.

If DM belongs to a mirror sector, where each ordinary particle is assumed to have a corresponding dark partner, it generally does not equilibrate with ordinary matter via the strong force, but nevertheless accrues in NSs due to gravitational interactions. This leads to matter in NSs being characterized by two pressures and two energy densities for each of the components (normal and mirror). Consequently, observable properties such as the M-R curves shown in figure 141 depend not only on the nuclear EOS but additionally on the dark matter parameters, i.e. $M(R)$ becomes an envelope of a neutron+DM $M(R)$ region in a two-dimensional plane [3326]. Similar results apply to the tidal deformability vs. mass curves. The width of the "line" in tidal vs. mass or radius vs. mass diagrams can be used to constrain DM properties in this scenario.

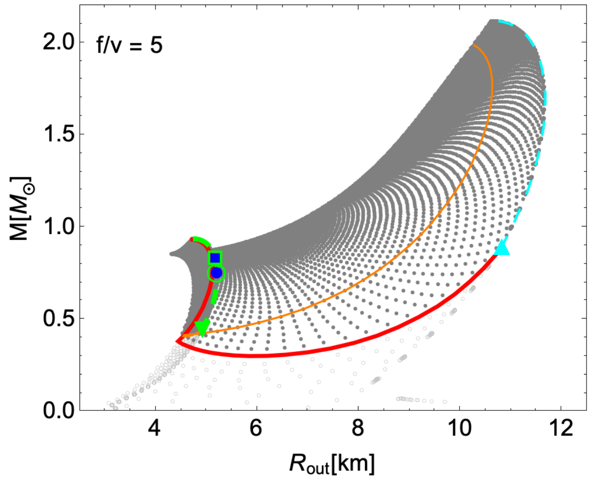

Figure 141. If mirror DM is added in varying quantities to ordinary NS matter, the admixture is equivalent to having a one-parameter family of EOSs, and observable to observable diagrams such as $M(R)$ or $\Lambda(M)$ are now populated in two dimensions, with pure NS matter providing the (cyan online) upper right edge of the figure. Reprinted figure with permission from [3326], Copyright (2023) by the American Physical Society.

Another proposed BSM phenomenon is an axion cloud surrounding NSs [3327]. While the motivation for axions in the context of the Strong-CP Problem is currently being debated [3328–3330], many kinds of light DM particles can create an extended halo around the star that increases the total gravitational mass. By contrast, heavy DM tends to condense in a core, leading to a smaller radius and tidal deformability compared to a pure baryonic star due to the additional gravitational pull. Figure 142 illustrates these two scenarios considering the asymmetric fermionic DM that interacts with the visible sector only through gravity [3331]. The outermost radius of the two configurations are different, as is the tidal deformability. Consequently, DM distributed in a halo/core could mimic an apparent stiffening/softening of strongly interacting matter EOS and spoil astrophysical constraints at high densities [3332, 3333]. This degeneracy between the effect of DM and strongly interacting matter properties at high densities could potentially lead to misleading conclusions and remains to be studied in detail.

The contribution of the next-generation GW telescopes is important in breaking a possible degeneracy between the effects of DM and strongly interacting matter at high densities. Along with advances in subatomic theory and experiment, astrophysical observations of NSs, and their thermal evolution require simultaneous efforts in setting bounds on the microscopic DM parameters [3338]. Thus, for popular particle-like DM models with mass $m_{\mathrm{DM}} \in (1, 10^4)$ GeV, accounting for the impact of DM on the star sequence leading to NS $\to$ BH collapse should allow constraining the nucleon-DM cross-section $\sigma_{N-\mathrm{DM}}$ to the 10^{-48} to 10^{-50} cm^2 range [1965]. This approach is competitive with other experiments, even below the solar system neutrino floor. Therefore, we emphasize the importance of combining multi-messenger data on NS properties with microscopic nuclear input and DM distribution in the target galaxy to address this question.

JCAP03(2026)081

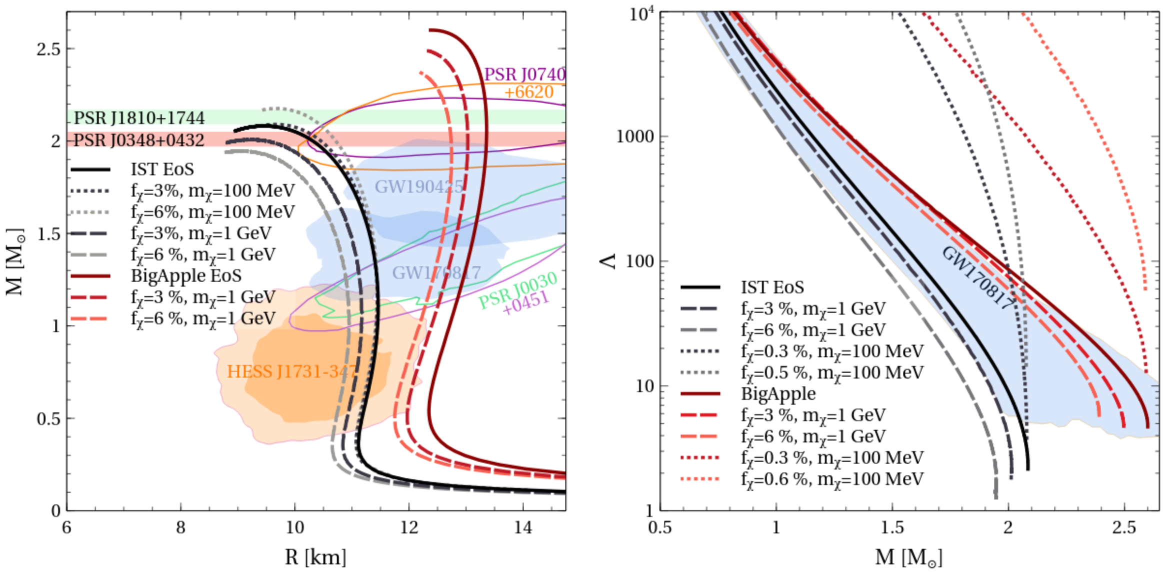

Figure 142. Modifications of the mass-radius relation (left panel) and tidal deformability of NSs with a fraction of DM, f_χ, and DM particle's mass, m_χ. To address the uncertainties of the baryonic matter EOS, the soft IST EOS [3334] (black solid curve) and stiff BigApple EOS [3335] (dark red solid curve) are considered. The 1σ constraints from GW170817, GW190425, the NICER measurements of PSR J00030+0451, and PSRJ0740+6620, as well as mass measurements of heavy radio pulsars (PSR J1810+1744, PSR J0348+0432) are plotted. The 1σ and 2σ contours of HESS J1731-347 [3336] are shown in dark and light orange. Figures reproduced from [3332]. The Author(s). CC BY 4.0 (left) and reproduced from [3337]. The Author(s). CC BY 4.0 (right).

7.4.3.3 The effect of dark matter on the merger dynamics. Binary NS coalescences provide a new and sensitive indirect way of constraining the properties of DM, as the GW signals contains information on their environment, where effects such as dynamical friction or accretion could change the signals away from those in vacuum. The environments of merging binaries could be different depending on the particular galaxy, the distance to the centre, and the shape [3315] of the galactic DM halo. Studies of the impact of DM on the post-merger phases of the binary NS system showed that DM cores can lead to additional peaks in the post-merger GW spectrum [3339] (and formation of a one-arm spiral instability [414, 415]). The extra spectral peak (or two for unequal masses), which occurs at higher frequency than the main post-merger peak associated to the rotation of the hypermassive remnant, provides a possible way to disentangle DM from nuclear EOS effects. It is found to arise from the fact that, while the normal matter components of two NSs merge, the compact DM cores are still orbiting within the remnant and take more time to coalesce [3339]. The location and features of the spectral peaks are expected to correlate with properties of the merging DM cores [3339], and may enable inferring their size. Constraining the DM core size then allows to more confidently extract the information about the nuclear matter. Moreover, simulations have indicated that due to the absence of non-gravitational interactions, the DM cores and the surrounding post-merger matter likely exhibit distinct rotational frequencies immediately after the merger. Over time, these frequencies might synchronize through gravitational angular momentum transfer, including tidal effects [3326]. The first two-fluid NR simulations

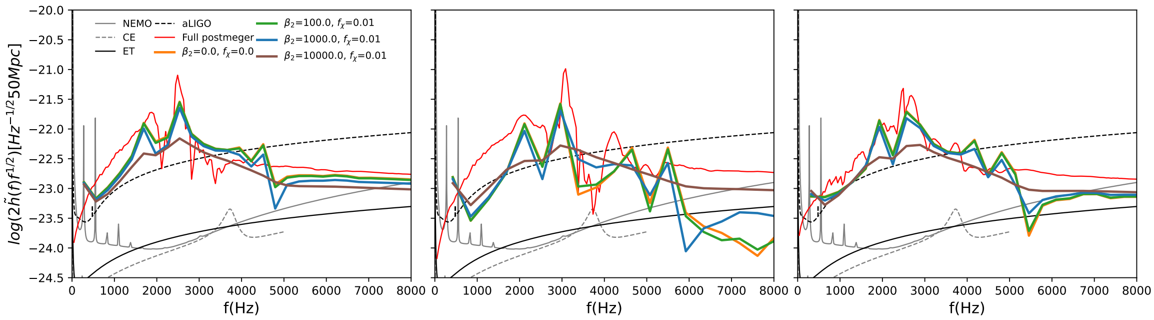

Figure 143. Spectral density computed for the full post-merger data (thin red line) and for the early post-merger interval (thick colored lines) obtained from variation of DM mass fraction f_χ and viscosity parameter β_2 defined as the coefficient of an effective velocity-dependent dissipative force $\sim \beta_2 v^2$. We also plot sensitivity curves of the NEMO, CE, ET, and Advanced LIGO detectors (black and grey curves). CoRe database [3267] sets THC005, THC0032, and THC0040 appear in the left, center, and right plots, respectively. The damping of the peak amplitude due to DM can be seen. Distance fixed to $d = 50\,\mathrm{Mpc}$. See ref. [3323]. Reproduced from [3323]. CC BY 4.0.

of NSs mixed with mirror DM, concluded that DM might prolong the inspiral phase as the amount of DM increases as well as decrease the kilonova ejecta [413].

Recently, DM models deployed in NS physics also have incorporated possible DM self-interactions, as suggested by galactic dynamics, as DM most likely flows with an effective viscosity [3323]. In the power spectral distribution, this damps the peak amplitudes at the frequencies of the (expected) main modes in the power-spectrum distribution, see figure 143 for selected CoRe database BNS merger simulations. ET, among other detectors, will better constrain whether such damping is at work.

To have a comprehensive understanding of the effect of DM, it is necessary to perform binary NR simulations and analyze kilonova ejecta [3340]. These simulations should encompass various DM candidates, particle masses, interaction strengths, and fractions. Furthermore, a thorough investigation should include a comparison with GW and electromagnetic signals.

To conclude this subsection, we stress that extracting an EOS or other properties of nuclear matter from ET data is always subject to a hypothesis about the gravity theory. To prevent misleading conclusions, the possible degeneracies need to be studied in detail, in particular: (a) impact of exotic matter (whose effect is to soften/stiffen the EOS, modify the merger outflow, kilonova ejecta, and electromagnetic counterpart) and (b) degeneracies with modifications of General Relativity (which needs to be simultaneously tested with NS data).

7.5 Executive summary

As exposed throughout this section, the science potential for subatomic physics with GWs from next-generation observatories such as ET will be immense and is poised to enable groundbreaking advances in the fundamental understanding of the structure of NSs, dense hadronic matter, and the QCD phase diagram. Among others, copious detections of GWs from BNS and NSBH systems are guaranteed. Rapid progress is underway to face computational and modeling challenges and those for interdisciplinary interactions, such as optimally benefiting from the opportunities offered by GW astronomy. Here we will summarize the

JCAP03(2026)081

main points discussed in this section, on the areas where ET's capabilities will lead to advances in our understanding, the main challenges to be overcome and potential synergies with other facilities.

ET observables for probing subatomic physics

Different observable GW sources will probe different aspects of subatomic matter:

- Isolated mature NSs, and NSs in the inspiral phase of BNS mergers, can be considered as cold and in chemical (β-) equilibrium. From the inspiral phase of such mergers and the tidal disruption in NS-BH systems, NS properties such as radius and tidal deformability along with the underlying EOS for cold β-equilibrated matter can be recovered with great accuracy with a limited number of detections improving considerably on current knowledge, see section 7.3.1. A potential phase transition in dense NS matter is detectable for an onset at low densities from a few loud events, which will potentially also enable measuring subdominant matter effects such as those from characteristic oscillation modes.

- In a post-merger remnant, matter is heated up and higher densities are reached such that signals from the post-merger phase probe dense and hot matter. The complicated dynamics and the fact that matter is out of chemical equilibrium renders the interpretation of GW signals from this phase more difficult than during inspiral. Nevertheless, as discussed in section 7.3.2.1, the detection of such a signal in combination with the associated inspiral allows to obtain additional information on the EOS, for example on a potential phase transition at high densities.

- The GW signal from a CCSN is highly sensitive to the progenitor properties and the supernova dynamics. Nevertheless, GW asteroseismology of the newly born PNS can reveal properties such as its surface gravity and some features of hot and dense matter, see section 7.3.2.2 for more details.

- ET will be able to probe the deformations of hundreds of pulsars either detecting a signal, or setting constraints below the maximum ellipticity predicted by theory, and for tens of high frequency millisecond pulsars ET will probe ellipticities below 10^{-9}; see section 7.3.1.2 and section 8.

- In combination with other observables, e.g., electromagnetic counterparts of BNS or NSBH mergers, there will be additional information to place constraints on the EOS as well as on the formation of heavy elements. In particular, the improved sky-localization of future GW signals observed by ET will provide important information for follow-up searches of electromagnetic counterparts; see section 7.3.3 and section 5.

Challenges

In order to take full advantage of this scientific potential for nuclear physics with ET, important theoretical, numerical, and computational challenges remain to be resolved.

- A key feature of GW measurements is that they are based on cross-correlating theoretical models with the data to make the link between the signals and the fundamental source physics. Models for NS binary systems that include more realistic physics are urgently needed for data analysis; the specific aspects requiring prioritized efforts for subatomic physics were highlighted throughout this section. This also requires key inputs from nuclear physics on the possible matter properties beyond the pressure-density relationship, such as finite temperature effects and transport coefficients (see section 7.2.3), from studies that follow a first-principle methodology as far as possible. Interactions between the GW and nuclear-physics communities are essential to communicate what information is required and what formats of the results are most useful as inputs for numerical simulations and analytical studies. Efforts are also necessary to develop suitable waveforms for data analysis that include NS matter effects (see section 7.4.1).
- On the computational side, the complex merger process in BNS events requires NR simulations with high computational cost on supercomputers. At present, they remain limited in length, resolution, parameter space coverage, and microphysical realism, see the discussion in section 7.4.2. NS binary signals for ET will linger for several hours in the sensitive band, which also presents a computational challenge for data analysis. With current methods and infrastructures, it will become prohibitively expensive. New tools such as deep learning could help address this critical issue; see section 11.
- In this context, it should also be noted that the extraction of nuclear matter properties is simultaneous with constraining modifications of GR and exotic (perhaps dark matter) components of NSs, which can mask or distort the subatomic effects and that further work is required to understand resulting degeneracies and develop strategies to mitigate them, as discussed in section 7.4.3. A better and independent understanding of the underlying nuclear physics from theory and experiment will open new avenues for tests of gravity, cosmology, and explorations of dark matter with GWs from NS events.

Synergies with other facilities

In addition, to optimize the science payoffs with GWs for nuclear physics requires strengthening the efforts on interdisciplinary connections with various other probes from astrophysical observations, and nuclear physics theory and experiment, see section 6 for more details. As an example, as discussed in section 7.3.1, from the inspiral of BNS mergers, the cold β-equilibrated EOS can be determined accurately, but without additional information it is difficult to determine matter composition or properties of symmetric nuclear matter. Only a combination of data from different probes will enable pinning down the forces acting in dense matter. In particular:

- Heavy-ion collisions at lower energies probe the EOS of warm dense matter and yield valuable information in a regime of density and isospin asymmetry different from NSs; data on nuclear masses, excitations, resonances, and the determination of the neutron skin thickness probe properties of nuclear interactions in yet other complementary realms than NSs. Likewise, it will be important to exploit experiments to gain insights into the complex physics of kilonovae, for instance, by measuring masses of exotic nuclides and synthesizing neutron-rich nuclei with rare isotope beam facilities.
- New electromagnetic telescopes will also come online in the next years, for some of which an important objective is to observe counterparts to GW events in different wavelengths. In addition, X-ray telescopes, such as e.g., NICER or the planned Strobe-X, and radio-timing, e.g., with SKA and its precursors, will provide information on NS masses and radii complementary to BNS and NSBH inspirals. Multi-messenger observations of (P)NS cooling will allow us to gain valuable insight into the composition of the dense (and hot) matter in these compact stars.

8 Stellar collapse and rotating neutron stars

Stellar collapses are among the most powerful astrophysical phenomena, in which extreme temperatures and densities are reached. They are characterized by complex physical processes, involving hydrodynamics, magnetic fields, neutrinos, nuclear physics, electromagnetic and gravitational radiation. The final remnant of a stellar collapse is a compact object, namely a neutron star or a black hole.

Although some aspects are still not totally clear, stellar collapses are unanimously considered as potential sources of gravitational-waves (GWs). GWs are associated both to the collapse itself, in the form of transient emission, and to the collapse aftermath in the form of persistent emission from an asymmetric neutron star, isolated or part of a binary system. Further possible channels of GWs include various kinds of dynamical instabilities, which can set in during the early stages of the remnant life, and glitches, likely associated to cracks in the neutron star crust or to the interplay among the crust and the inner superfluid.

In this section, we describe the main aspects of the collapse process and of the resulting neutron star, focusing attention on the associated GW emission in view of the unprecedented sensitivity promised by Einstein Telescope. Benefits of the multi-messenger approach, in which information from electromagnetic, neutrino and GW observatories are combined, are also stressed both in terms of improved detection capabilities and in terms of science return.

JCAP03(2026)081

8.1 Introduction

In this era of GWs as new and exciting astrophysical messengers, stellar collapses and the resulting neutron star (NS) will play a crucial role. Their emission encompasses all the available multi-messenger tracers: electromagnetic (EM) waves, cosmic rays, neutrinos, and GWs. They are unique laboratories where the most extreme phases of matter can be studied: not only probing extreme regimes of gravity and electromagnetism but also the strong and weak interactions can be studied in regimes that there is no hope to explore on Earth. To interpret at the best future GW detections, it is necessary to consolidate our understanding of the stellar collapse mechanisms and of the different NS classes, their EM and neutrino signatures, rates and the expected GW characteristics.

Concerning GW emission, stellar collapses are predicted to emit short bursts of radiation, with duration from a few milliseconds to a few seconds, associated to the core bounce and following explosion, with a more structured emission due to the excitation of oscillation modes of the newly formed proto-neutron star (PNS). NSs have been predicted to emit short GW transients in response to sudden changes in the star's mass quadrupole, like glitches, and persistent signals due to long-lived deviations from an axi-symmetric shape. Young NSs could also be subject to the excitation of various kinds of oscillation modes triggered by dynamical instabilities or following fast processes, like crust cracks or rearrangements of the star's magnetic field.

Overall, stellar collapse events detectable by ET will belong to the Milky Way or the local group of galaxies (i.e. within a few Mpc), with the possible exception represented by long-transient emission from fast spinning newborn magnetars endowed with a super-strong inner magnetic field, which could be detectable up to a distance of a few tens of Mpc.

In this section, we will briefly discuss the different data analysis techniques required to detect the GWs emitted by such sources.Depending on their characteristics, different data analysis algorithms are needed to extract the signals from detector data. In general, the development of suitable data analysis methods must conform, as much as possible, to three keystones: *sensitivity*, *robustness* and *computational efficiency*. On one hand, search algorithms must be as sensitive as possible to the specific kind of GW signal being searched. On the other hand, these algorithms must often balance search sensitivity to generic, unmodeled signal features with robustness against detector noise artefacts.In addition, analyses computational cost also play a relevant role and must be taken into account during method development.

Since in this section we deal with the outcomes of the stellar collapse, we begin in subsection 8.2 to recall the main evolutionary path of stars toward the collapse and discuss the limiting masses of stars that explode and those that collapse directly to a black hole (BH). We also discuss the minimum mass of stars that enter the pulsation pair instability exploding, therefore, as Pair Instability Supernovae leaving no remnant. We also address the dynamics of the explosion of core collapse supernovae, the current status of their observations and the expected GW and neutrino emission from these objects. We provide the observed and expected core collapse supernova rates (CCSNR) and in particular the expected rate in the Milky Way, which is of key importance to plan the observational strategy for the current and next generation GW and neutrino detectors.

JCAP03(2026)081

In subsection 8.3, we outline NSs' main features, in terms of structure, and emission of EM radiation, going from steady beamed radio or gamma emission of pulsars to burst-like highly energetic X- or gamma-ray flares in young magnetars. Moreover, we describe the main mechanisms through which NSs are expected to emit GWs. We are here mainly interested in isolated NSs, or NSs in stellar binary systems like Low Mass X-ray Binaries (LMXBs) and pulsars in binary systems, in which the GW emission is powered by the NS rotational energy rather than the orbital (as for coalescing binaries, discussed in section 6).

Subsection 8.4 is devoted to a discussion of GW detection prospects of the aforementioned sources and to outline the role of EM and neutrino future facilities in the context of multi-messenger astronomy. A brief classification of the main search categories is also presented for both stellar collapses and rotating NSs GW signals. Moreover, some basic information on the main analysis methods is given, stressing possible open points to be tackled in view of ET and promising routes for improvement.

8.2 Stellar collapse

8.2.1 Stellar evolution toward stellar collapse

In the general picture of stellar evolution stars with initial mass M $\gtrsim$ 10 $M_\odot$ never experience a significant electron degeneracy in the core during all their nuclear burning stages; therefore, they evolve to higher and higher temperatures, fusing heavier and heavier nuclei until an iron core is formed. The iron core, then, becomes unstable, collapses and through a sequence of events drives the explosion of the star as a core collapse supernova (CCSN) (see section 8.2.2). However, as the initial mass increases the explosion becomes harder and it is expected that above a critical initial mass the stars, at the end of their evolution, will collapse directly to a BH, producing a so-called failed explosion. As the progenitor mass increases even more, the core of these stars becomes unstable for pair creation, it collapses and eventually drives a pair instability supernova (PISN) that leaves no remnant. The minimum masses of the stars that produce a successful explosion, $M_{\rm CCSN}$, a direct collapse (DC) to a BH, $M_{\rm DC}$, and a PISN, $M_{\rm PISN}$, depend in general on the initial metallicity and rotation velocity. In general $M_{\rm CCSN} < M_{\rm DC} < M_{\rm PISN}$.

According to the most recent studies [3341], stars with mass $M \lesssim 7.5\ M_\odot$ evolve along the Thermally Pulsing Asymptotic Giant Branch (TP-AGB) phase and end their life as CO White Dwarfs (CO-WDs). Stars with $M \gtrsim 9.2\ M_\odot$, on the contrary, evolve through all the major stable nuclear burning stages and eventually explode as CCSN leaving a compact remnant, i.e. either a neutron star or a BH. Therefore, according to this study $M_{\rm CCSN} \sim 9.2\, M_\odot$. However, the minimum mass that produces an explosion cannot be set to such a value because stars in the range $\sim (7.5 - 9.2)\ M_\odot$ have a much more complex evolution and a fraction on them can eventually explode as electron capture supernovae (ECSNe). In particular, as a result of the carbon burning phase, stars in this mass range develop a degenerate ONeMg core and enter the thermally pulsing phase. These stars are usually called Super Asymptotic Giant Branch (SAGB) stars. Among them, the most massive ones, $\sim (8.5 - 9.2)\, M_\odot$, achieve central densities close to the threshold density for the activation of the electron capture (EC) $^{20}\mathrm{Ne}(\mathrm{e}^-, \nu)^{20}\mathrm{Fe}$. Once such an electron capture becomes efficient, deleptonization and thermonuclear instability develop and may eventually lead to the ECSN. The final fate of

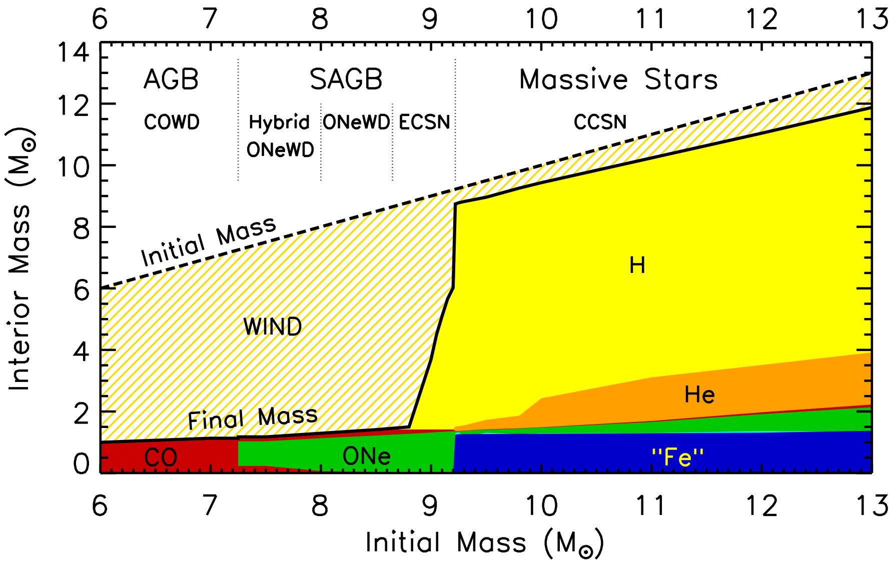

Figure 144. Final fate of stars in the mass range $(7-13)\,M_\odot$ according to [3341].

such stars however is not yet completely well established since it depends on the competition between the energy released by the nuclear burning front and the loss of pressure due to the deleptonization occurring in the central zones. If the energy released by nuclear burning prevails, degeneracy is removed and the star explodes as a thermonuclear ECSN [3342–3345]. If, on the contrary, the deleptonization dominates, the collapse cannot be halted and the star collapses into a NS (core collapse ECSN) [3118, 3342, 3344, 3346–3349]. Which outcome is realized from ECSNe depends on both the details of the modeling of the presupernova evolution and explosion. For all these reasons the minimum mass that can produce an explosion as an ECSN cannot be identified with certainty of precision and we can only say that it is in the range $M_{\rm ECSN} \sim (8.5-9.2)\,M_\odot$. A summary of the evolution and final fate of stars in the mass interval between 7 and 13 $M_\odot$ is shown in figure 144.

For sufficiently high masses (with $M > M_{\rm CCSN}$), the binding energy of the stars are so large that they do not explode but, rather, collapse directly to a BH. The determination of the minimum mass that produces a direct collapse to a BH ($M_{\rm DC}$) is quite difficult because it depends on the details of the explosion and in particular on the amount of fallback of material and mixing occurring at late times. After about three decades of research, the current reference model for CCSNe is based on the "delayed shock mechanism" or "neutrino-heating mechanism", which was originally proposed by Wilson and Bethe [3067, 3081, 3350–3355]. However, state-of-the-art 3D simulations of the explosion, which include the most sophisticated treatment of neutrino transport, cannot follow the explosion at late times ($t \gtrsim 10$ s), when most of the fallback should occur, because of the tremendous cost of computer time. As a consequence these simulations cannot accurately predict the final mass of the compact remnant and whether the supernova (SN) will be successful or failed, in the entire SN progenitor mass range [3079, 3082, 3356–3364].

A simplified approach for studying the explosion of massive stars is to artificially stimulate the SN explosion by injecting some amount of energy at an arbitrary mass coordinate in the

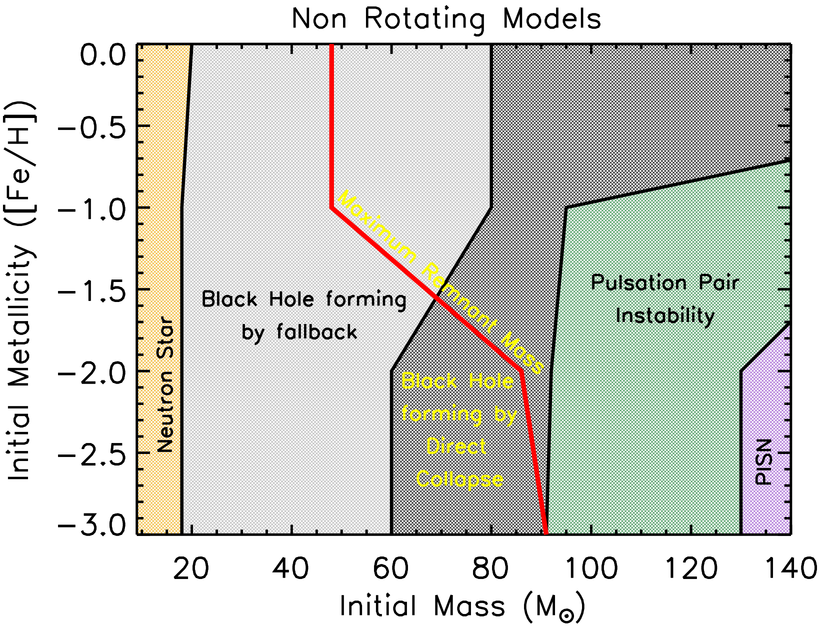

Figure 145. Final fate and remnant masses predicted for non rotating stars as a function of the initial mass and initial metallicity. The red line marks the predicted maximum remnant mass.

progenitor model. This extra energy induces the formation of a shock wave whose propagation through the mantle is followed by means of a hydro code. Different groups adopted different schemes to inject the extra energy: a thermal bomb [3365]: a piston [3366]: a kinetic bomb [3367]: thermal energy due to a calibrated neutrino luminosity [3368]. Whichever is the way in which the energy is deposited into the presupernova model, the typical evolution of the explosion involves (1) an initial remnant; (2) a shock wave propagating through the mantle and inducing compression, heating, explosive nucleosynthesis and expansion of the shocked material; (3) a fallback of the deepest layers of the expanding mantle because of the gravitational field of the compact initial remnant; (4) a mass cut which is the mass separation between the ejecta, which will have a given final kinetic energy, and the final remnant, which in general will be larger than the initial one. The main advantage of this approach is that the computing cost is relatively small. Thus, it is possible to follow the evolution of the shock over longer timescales and to estimate the amount of fallback and the final remnant mass. The 1D approach has been extensively used to study the chemical composition of the ejecta produced by SN explosion, especially in the context of explosive nucleosynthesis. A recent calculation of the explosion of an extended set of presupernova models in the range $(13-120)\ M_\odot$, with initial metallicities corresponding to $[\mathrm{Fe/H}] = 0,\ -1,\ -2,\ -3$ and initial rotation velocities $v = 0,\ 300$ km/s, in the framework of the thermal bomb, has shown that: (1) for non rotating models the threshold main sequence masses above which the stars undergo a direct collapse to BH are $M \simeq 60\ M_\odot$ for $[\mathrm{Fe/H}] = -2,\ -3$ and $M \simeq 80\ M_\odot$ for $[\mathrm{Fe/H}] = 0,\ -1$; (2) for stars with initial rotation velocity $v = 300$ km/s the transition from a successful SN explosion to a direct collapse to BHs occurs for initial main sequence masses of $\simeq 30\ M_\odot$, $\simeq 17\ M_\odot$, $\simeq 15\ M_\odot$, and $\simeq 15\ M_\odot$, for $[\mathrm{Fe/H}] = 0,\ 1,\ 2,\ 3$, respectively. A summary of these results are shown in figures 145 and 146.

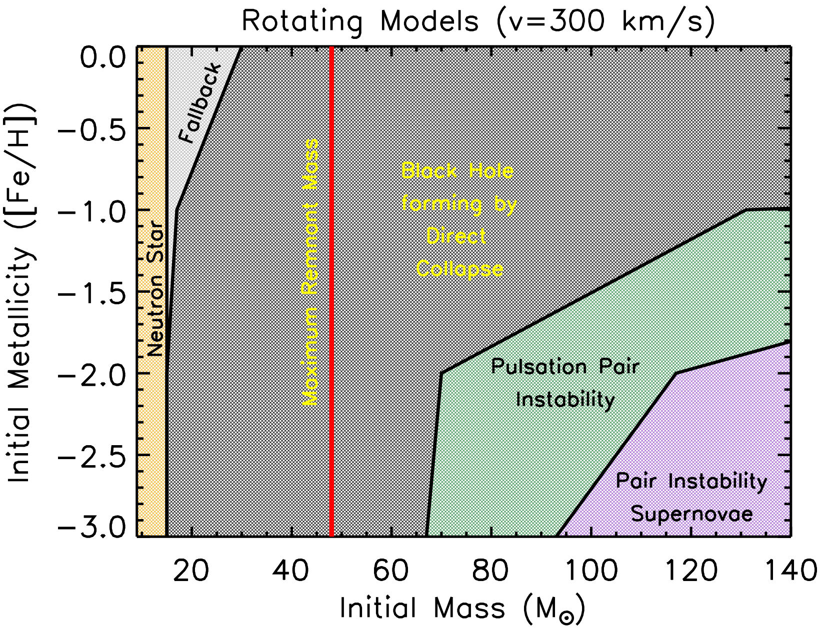

Figure 146. Final fate and remnant masses predicted for stars with initial rotation velocity of 300 km/s as a function of the initial mass and initial metallicity. The red line marks the predicted maximum remnant mass.

Above a given threshold value of the initial mass, or more correctly of the CO core mass, after core He burning the stars evolve at sufficiently high temperature and low density (i.e. high central entropy) that electron-positron pairs are created copiously, converting internal energy into rest mass of the pairs without contributing much to the pressure. When the star enters this stage the equation of state softens, the structural adiabatic index decreases below 4/3 and the core becomes unstable. This is the "pair-instability" [1791, 1792, 3369]. According to [1790], if the mass of the CO core is larger than $\sim 53\ M_\odot$, this instability results in a dynamical collapse of the core that triggers explosive oxygen and silicon burning. These nuclear burning produce enough energy to revert the collapse leading to the explosion of the star as a PISN. Unlike other types of supernovae, the explosion mechanism of a PISN is well understood, without complications like mass cut or fallback. If, on the contrary, the mass of the CO core is in the range $\sim (35 - 53)\ M_\odot$, the nuclear burning are not sufficiently energetic to disrupt the star but, rather, they induce a series of pulsations. This is the "pulsation pair-instability". After a number of pulsations the H rich envelope is almost completely lost and the core of the star resumes the classical evolution of a typical massive star eventually collapsing to a BH (PPISN). In general the limiting masses that eventually become PPISN or PISN, depend on the initial metallicity and initial rotation velocity. According to recent studies [3370], for solar metallicity models, regardless of the initial velocity, the mass loss is efficient enough that the CO core never becomes massive enough to enter the pair instability regime. For non-rotating models of lower metallicities, on the contrary, the mass loss is almost negligible, in this way $M_{\rm PPISN} = 95,\ 92,\ 91\ M_\odot$ and $M_{\rm PISN} = 163,\ 130,\ 130\ M_\odot$, for metallicities [Fe/H] $= -1,\ -2,\ -3$, respectively. The effect of rotation is that of increasing the CO core mass due to the rotation driven mixing, as a consequence for rotating models with initial velocity of 300 km/s the limiting masses are $M_{\rm PPISN} = 131,\ 70,\ 67\ M_\odot$ and $M_{\rm PISN} = 235,\ 117,\ 93\ M_\odot$, for metallicities [Fe/H] $= -1,\ -2,\ -3$ (see figures 145 and 146).

The most massive BH ($M_{\rm BH,max}$) that can be formed corresponds to the mass of the most massive stars that collapses directly to a BH. For non-rotating stars $M_{\rm BH,max} \simeq 91\ M_\odot$ and is the result of the direct collapse of the most massive star at [Fe/H] $= -3$ not undergoing PPISNe (red line in figure 145). In the case of rotating stars (with initial rotation velocity of 300 km/s), because of the enhanced mass loss driven by rotation, even if more stars collapse directly to a BH, $M_{\rm BH,max}$ is lower than for non-rotating stars. In particular, in the rotating case $M_{\rm BH,max} \simeq 47\ M_\odot$ and is the result of the direct collapse of a star undergoing PPISNe, according to the PPISNe models of [1790].

An important aspect of the progenitors of a CCSNe is the presence of an extended H-rich envelope. The basic classification of CCSNe in Type IIP, Ib and Ic, in fact, is based on the presence of hydrogen in their ejecta (see section 8.2.4). During the presupernova evolution, stars with initial mass larger than $M \sim 20\,M_\odot$ lose a substantial amount of mass. Stars above a critical mass, then, lose their entire H-rich envelope and become Wolf-Rayet (WR) stars. The limiting masses that form the various kinds of WR stars (the classification of a WR star is based on the chemical composition of their atmospheres) depend on the interplay between the evolutionary times and the efficiency of mass loss. A detailed survey of massive stars in a wide range of initial masses, metallicities and rotation velocities [3370] has shown the following results. At solar metallicity, non-rotating stars populate the Red Super Giant (RSG) branch up to a luminosity $\mathrm{Log}(L/L_\odot) \sim 5.7$, which corresponds to a mass of $\sim 40\ \mathrm{M}_\odot$. More massive stars lose a major fraction of their H-rich envelope because they overcome the Eddington luminosity before reaching the RSG branch and hence turn back blueward where they spend all their core He-burning lifetime. Stars in the mass range $\sim$ 20–40 $M_\odot$ leave the RSG branch during the core He burning and evolve towards a Blue Super Giant (BSG) configuration, eventually becoming WR stars. Stars with initial mass $M \lesssim 15\ M_\odot$, on the contrary, remain RSG until their final explosion. Accordingly, the expected maximum mass for the progenitors of SNIIP is $M_{\rm IIP} \sim 17\ M_\odot$ (which corresponds to a maximum luminosity of $\mathrm{Log}(L/L_\odot) \sim 5.1$). Moreover, stars with initial mass $M \gtrsim 25\ M_\odot$ loose their entire H-rich during the RSG phase and therefore are expected to explode as SNIb. Stars in the range $\sim (20 - 25)\ M_\odot$ retain a modest amount of H in the envelope at the presupernova stage and therefore should explode as SNIIb. Since the transition SNII/SNIIb/SNIb is not yet clear either from the theoretical and observational side, we can consider only one limiting mass $M_{\rm IIP} \sim 17\ M_\odot$ such that stars with $M < M_{\rm IIP}$ explode as SNII while stars with $M > M_{\rm IIP}$ explode as SNIb. These limiting masses are in fair agreement with some observed properties of massive stars: (a) $M_{\rm IIP} \sim 17\ M_\odot$ is compatible with the lack of detected progenitors (of SNIIP) with luminosities higher than $\mathrm{Log}(L/L_\odot) \sim 5.1$, as reported in [3371] — therefore this result constitutes a natural possible explanation of the so called “RSG problem” [3372]; (b) in a scenario in which all the stars with $M > 25\ M_\odot$ fail to explode and collapse directly to a BH, no SNIb is expected at luminosities larger than $\mathrm{Log}(L/L_\odot) \sim 5.6$ — this result is at least not in contradiction with the 14 SNIb progenitors with no detection reported in [3371], moreover, the expected amount of mass ejected by stars exploding as SNIb is of the order of $M_{\rm ejecta} \sim 6\ M_\odot$, i.e., in rather good agreement with the ejected masses of

$(3-4)\ M_\odot$ estimated from the SNIb light curve fitting (see, e.g., [3373]). The effect of rotation is in general that of reducing both the maximum mass of stars that evolve, with a significant fraction of their lifetime, as RSG and the minimum mass that becomes WR. In particular, solar metallicity models, with initial rotation velocities $v \geq 150$ km/s, are expected to populate the RSG up to a luminosity of the order of $\mathrm{Log}(L/L_\odot) \sim 5.5$ and then to explode as SNIb ($M_{\rm IIP} \sim 13\ M_\odot$).

At metallicity corresponding to [Fe/H] $= -1$, in the absence of rotation, the strong decrease of the mass loss raises the maximum mass that settles on the RSG branch up to $\sim 25-30\ M_\odot$. The more massive ones, on the contrary, do not reach the RSG branch before the explosion because these stars turn towards their Hayashi track on a nuclear timescale. Therefore, at this metallicity, without rotation, RSG SNIIP progenitors are predicted with masses as high as $\sim (25-30)\ M_\odot$; above this value stars are expected to explode as BSGs SNIIP. Given the very low amount of mass lost at this metallicity, only stars with initial mass $M \geq 80\ M_\odot$ may become WR, therefore in this case $M_{\rm IIP} \sim 80\ M_\odot$. At lower metallicities ([Fe/H] ≤ -2) also the less massive stars turn to the red on a nuclear timescale so that basically no stars are expected to populate significantly the RSG branch at these metallicities. This does not imply that no RSG SNIIP are expected, because stars in the range $\sim (13-25)\ M_\odot$ reach the RSG branch towards the end of the core He burning. Given the extremely low amount of mass lost by these stars, all of them explode as SNIIP (blue or red supergiants). The main effect of rotation at these (low) metallicities is that of pushing the stars towards the RSG branch. As a consequence, low metallicity rotating stars with $M \lesssim (25-30)\ M_\odot$ spend a considerable amount of time on the RSG branch where they eventually explode as RSG SNIIP. The more massive ones, on the contrary, approach their Eddington luminosity when their surface temperature drops to Log $[T_{\rm eff}\ ({\rm K})] \sim 3.8-4.0$, lose a huge amount of mass and turn to the blue becoming WR stars. As a consequence, at subsolar metallicities the limiting mass between SNIIP and SNIb for rotating models is in the range $M_{\rm IIP} \sim (25-30)\ M_\odot$. Though no progenitor for SNIIP as massive as $(25-30)\ M_\odot$ has been detected yet, the present results imply the existence of these massive RSG progenitors (and SNIIP) at low metallicities and we expect their detection in the next future.

A summary of the limiting masses discussed in the previous paragraph is reported in table 13.

8.2.2 Modelling, explosion mechanisms, and dynamics

Besides the aforementioned stellar models our understanding of the dynamics of stellar core collapse owes a great deal to a growing set of ever more sophisticated numerical models (for recent reviews and works, see, e.g., [1757, 3106, 3355, 3363, 3374–3376]). The phase during which the GWs detectable by ground-based interferometers such as ET are emitted is only a short window of a few seconds in the wider sequence of events that transforms a star in hydrostatic equilibrium into a compact object. It is dominated by a very specific combination of input physics that differs from the stages before and after and thus calls for highly specialized methods for simulation and analysis. Primary ingredients for modelling are multi-dimensional and multi-scale (magneto-)hydrodynamics, relativistic gravity, the equation of state (EOS) describing matter at densities up to the supernuclear regime, reactions between

Metallicity [Fe/H]	Velocity (km/s)	$M_{\rm CCSN}$ ($\rm M_\odot$)	$M_{\rm IIP}^{**}$ ($\rm M_\odot$)	$M_{\rm DC}$ ($\rm M_\odot$)	$M_{\rm BH,max}$ ($\rm M_\odot$)	$M_{\rm PPISN}$ ($\rm M_\odot$)	$M_{\rm PISN}$ ($\rm M_\odot$)
0	0	9.2	17	80	47	-	-
0	300	9.2*	13	30	47	-	-
-1	0	9.2*	80	80	47	95	163
-1	300	9.2*	25	17	47	131	235
-2	0	9.2*	>120	60	89	92	130
-2	300	9.2*	25	15	47	70	117
-3	0	9.2*	>120	60	91	91	130
-3	300	9.2*	25	15	47	67	93

Table 13. Summary of the limiting masses. Values marked with * are obtained for the non rotating solar metallicity case; values marked with ** are obtained during the presupernova evolution and hence do not take into account the stars that directly collapse to a BH.

nuclei and between matter and neutrinos, and the transport of neutrinos from an opaque core to the transparent stellar envelope.

The main drivers of computational costs come from the neutrino sector [3363] where the direction dependence of the neutrino distribution and the energy dependence of the interactions with matter have to be taken into account, thus increasing the dimensionality of the problem beyond the usual three spatial and one temporal dimensions. Ideally, the Boltzmann transport equation for the neutrino distribution function in seven-dimensional phase space coupled to the equations of fluid dynamics would have to be solved. Additionally, the development of small-scale turbulence and the many dynamical time scales over which the cores have to be simulated increase the effort. Therefore, groups working on the field can perform state-of-the-art simulations at moderate rates of typically a few models per year (see, e.g., [1757] for a particularly extensive set of 3d models). Thus, many studies addressing specific questions on, e.g., the nature of the GW emission, employ approximations in one or several of these fields such as simplified neutrino schemes, e.g., expansions of the Boltzmann equations in angular moments, or a reduced dimensionality. Of particular interest for studying the GW signal might be that the moderate compactness of the cores and the lack of backreaction of the GW emission on the dynamics make meaningful results possible with post-Newtonian approximations, including calculating waveforms with the quadrupole formula, instead of a fully general relativistic treatment [3377–3379].

Beyond the technical difficulties related to computational costs, modellers have to contend with several physical uncertainties. A principal concern is the possible impact of neutrino flavor oscillations for which the lack of tight experimental and theoretical constraints still leaves a large parameter space to be explored [3218, 3380–3383]. Further microphysical uncertainties come from the nuclear EOS, in particular the potential transition to hyperons or quark matter at very high densities [3384].

The progenitor star arrives to the point of core collapse after having evolved through subsequent burning stages starting on the main sequence with the fusion of hydrogen to helium [1592, 3341, 3372, 3385–3387] (see also section 8.2.1). By then it has formed an

JCAP03(2026)081

onion-shell structure with an inert iron core of about a mass of $1.5\,M_\odot$ and a few 1000 km radius surrounded by layers composed of lower-mass elements. Once the core loses stability, it collapses within a few 100 ms to a PNS with a radius of initially around 50 km. While this qualitative picture is the same for all progenitors, with the possible exception of the supermassive stars formed at Cosmic dawn [1177], the precise structure of the core is still not fully understood. Important uncertainties arise from the necessary approximations made to model the evolution up to collapse. Spherically symmetric hydrostatic modelling is still and will for the foreseeable future remain the workhorse of stellar evolution theory. It can by design incorporate effects such as convection and other mixing processes, rotation, magnetic fields, or binary interaction only approximately. Modifications of the stellar profiles caused by these processes, however, can have crucial impact on the post-collapse evolution. Due to progress in numerical methods and computing power, traditional stellar evolution models are now supported by multi-dimensional MHD simulations of short episodes of, e.g., convective phases immediately prior to collapse, which makes it possible to test and calibrate approximate descriptions used to describe these effects [3376].

The PNS, composed of highly incompressible matter at supernuclear density, is close to hydrostatic equilibrium. Hence, the infall of surrounding shells of matter is abruptly stopped at its surface. These layers bounce back in the form of an outward moving shock wave. An intense burst of neutrinos streams out of the cores during the few ms that PNS formation takes and carry away the largest fraction of the energy released in the gravitational collapse. Thus weakened, the shock wave fails to leave the core and turns into an accretion shock located at a radius of between 100 and 200 km, having traversed less than $\approx 1\,M_\odot$ of core matter. The exterior layers, several $M_\odot$ of material, keep falling supersonically toward the center. If no additional processes entered the picture, the accretion would cause the PNS to grow in mass until it collapses to a BH in what amounts to a failure of the prompt explosion mechanism [2828].

Neutrinos are produced thermally in the hot and dense PNS and by the gas accreted onto it. They are in local thermodynamic equilibrium with matter inside the bulk of the PNS and start to decouple at the neutrinosphere marking its surface. They traverse a semi-transparent region extending up to the shock wave before freely streaming to infinity. Their mean energy, set by the temperatures at the neutrinosphere, exceeds that of the post-shock matter. Thus, reactions with matter will, on average, heat the gas at the expense of the neutrinos. If the energy transfer in this gain layer is sufficiently rapid compared to the velocity at which matter falls onto the PNS, it can unbind the gas from the gravitational pull of the PNS and thus cause an explosion marked by the shock revival and runaway to the stellar surface [3388]. The balance between the infall and the infrequent neutrino-matter reactions is too close to determine the outcome analytically. Detailed numerical models with accurate neutrino transport, however, show that this delayed neutrino-driven mechanism usually does not succeed in reviving the shock.

Multi-dimensional models show an increased heating efficiency because the fluid, no longer bound to travel on purely radial trajectories, can dwell for a longer time in a place where it is exposed to the neutrino flux, e.g., because it is caught up in a vortical flow [3389]. In the gain layer, such eddies are a natural consequence of the convective instability induced by

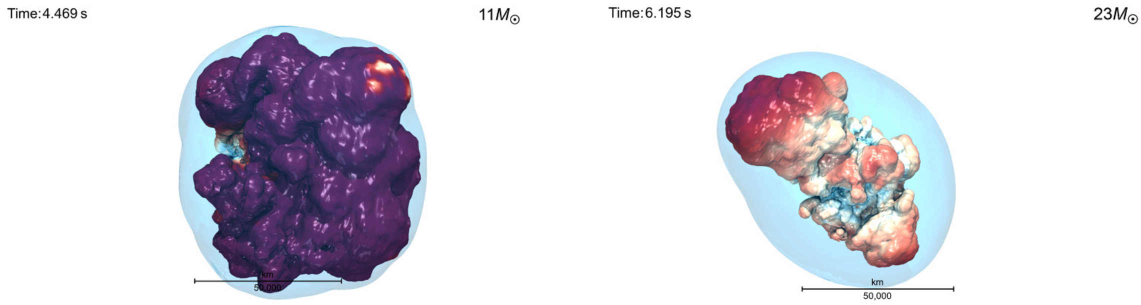

Figure 147. Morphology of the ejecta of two three-dimensional models of neutrino-driven SNe for progenitors of initial masses of 11 and 23 $M_\odot$ [3399]: isosurfaces of 10% abundance of ^{56}Ni colored by the Mach number of the radial velocity and, as blue veil, the shock surface. Reproduced from [3399].

neutrino heating [3390]. Further non-radial motions can be caused by the standing accretion shock instability (SASI) that leads to large-scale deformations of the shock and the enclosed matter [3356, 3391]. If these effects manage to revive the shock wave, it will start to propagate outward and eject in a very aspherical manner parts of the stellar material enriched with heavy elements produced before or during the SN (see figure 147). After breaking out of the stellar surface, a bright SN starts to shine electromagnetically, powered by the thermal energy of the gas and by the decay of newly produced radioactive isotopes.

The consequences of the multi-dimensional nature of the event go beyond the mechanism of shock revival. The hydrodynamic instabilities can transfer linear and angular momentum from the envelope to the PNS, thus giving it a non-zero kick velocity and spin [1824, 1892, 3392–3395]. Additionally, convection is also excited in the PNS where it enhances the neutrino emission (e.g., [3117, 3396, 3397]). The simultaneous presence of downflows and outflows behind the shock means that the PNS can continue to accrete even while the explosion is already proceeding.

That this hydrodynamically aided neutrino-driven mechanism can work in principle has been shown in two-dimensional axisymmetric and in fully three-dimensional simulations independently with many different numerical approaches (e.g., [3398]). Irrespective of currently open or discussed issues such as the explosions conditions depending on the progenitor properties, the role of different instabilities and of turbulence, the origin of the spin and kick velocity of the NS formed from the PNS, and of the difficulties to match simulations to an observed event, the current generation of models seem to offer a viable explanation for a large fraction of observed SNe (e.g., [1757, 3364]). They also indicate that this mechanism might have difficulties to produce more extreme explosions, in particular ones with above average kinetic (i.e., $E_{\rm kin} \gg 10^{51}$ erg) or EM energies, relativistic outflow velocities, or particular nucleosynthetic yields.

The main limitation of the neutrino-driven mechanism is the very loose coupling of the energy carried by neutrinos to the post-shock gas. The magneto-rotational explosion mechanism overcomes this restriction by invoking an alternative energy source for the powering outflows in the form of the rotational energy of a PNS spinning with periods in the ms range. The energy thus available is at $E_{\rm rot} \sim \mathcal{O}(10^{52})$ erg sufficient for events on the hypernova branch.

Sufficiently strong magnetic fields then act as very efficient conduits for transporting angular momentum outward and hence launching outflows at the cost of extracting rotational energy and spinning down the PNS [3400, 3401]. Multi-dimensional simulations have demonstrated the viability of this mechanism (recent work, e.g., [3078, 3083, 3085, 3402]). Apart from the high energies that can be reached, it differs from the standard mechanism by the potential to accelerate mildly relativistic jet-like outflows preferentially along the rotational axis. Apart from observed explosions with such characteristics, the existence of magnetars, i.e., a population of young NSs with extremely strong magnetic fields, suggests that the magneto-rotational mechanism works for a non-zero, yet so far poorly determined, fraction of stars. The uncertainty on the rates comes from our lack of knowledge about the internal rotation rates of potential progenitors and from the unsettled question as to how the cores reach the required strong magnetic fields. Compression during the infall and differential rotation will certainly increase the pre-collapse field strength, and additional amplification mechanisms such as convection and the magnetorotational instability can boost the field further [3071, 3403]. The latter, however, are connected to small-scale turbulence and, thus, not easy to follow in numerical simulations with limited resolution.

Other proposed explosion mechanisms rely on tentative modifications of nuclear physics at a few times the saturation density [3100, 3384, 3404]. A phase transition from ordinary matter to a state composed of u, d, s quarks can liberate enough energy to launch a successful explosion accompanied by a sudden increase of the PNS density and a burst of neutrino emission. Such a phase transition could power an explosion even if none of the other mechanisms worked, as in that case the PNS is bound to accrete large amounts of matter and contract to reach the threshold density. While the nuclear physics input is uncertain and somewhat speculative, simulations, so far mostly in spherical symmetry, have shown the principle viability. This result can be turned around to use searches for observations compatible with such an explosion type to put constraints on the properties of nuclear matter [3405].

In the absence of shock revival and jet formation, and sometimes even going together with them, the PNS can, by accretion of enough matter, transform into a BH. Even then, explosions can occur in the presence of rapid rotation. In the collapsar scenario [3406, 3407], an accretion disk would form orbiting the BH inside the core, i.e., composed of matter of subnuclear, but nonetheless very high density. Magnetic fields generated in the disk and/or neutrinos emitted by it can extract a large fraction of the gravitational energy released in the accretion process, and power collimated jets which, for sufficiently low ambient densities, can have highly relativistic velocities [3408]. As shown in multi-dimensional simulations, the outcome of such an evolution can be a long gamma-ray burst.

In most of the successful explosions, by far most of the released energy is carried away by neutrinos ($E_\nu \sim 10^{53}$ erg) over a period of several seconds. The kinetic energy of the ejecta is usually quoted with a canonical value of $E_{\text{kin}} \sim 10^{51}$ erg, but has a large scatter. The EM emission tends to be lower by roughly two more orders of magnitude. There is a basic consistency between observations and theory/simulations on these figures. For the energy emitted in GWs, the upper limits from the non-detections so far are not very tight. Theoretical results indicate that the GW emission is again several orders of magnitude less and thus dynamically insignificant. By probing the wide range of non-spherical motions

JCAP03(2026)081

described above, in particular PNS oscillations, rotation, and aspherical ejecta expansion, GWs nonetheless offer an intriguing possibility to directly learn about the dynamics in the core.

8.2.3 GW and neutrino emission

Neutrinos (for recent reviews, see, e.g., [3117, 3218, 3409]) and GWs share many characteristics as the only direct observables of the dynamics in the stellar core. However, they probe different and complementary aspects of the physics. Neutrinos are produced as a consequence of the release of gravitational and thermal energy and carry most of it from the core (see section 8.2.2). This property makes them primary probes of the energetics of the collapse and explosion. GWs, on the other hand, are only emitted in proportion to the breaking of spherical symmetry. Hence, not all processes necessarily leave an observable imprint in the GW signal. However, as outlined above, all cores will eventually develop pronounced anisotropies and thus produce GWs. In line with these different emission properties, the methods used for detecting and analysing neutrinos and GWs each have their own characteristics. For a sufficiently nearby explosion, neutrino detectors would collect large numbers of neutrinos, enabling us to reconstruct the neutrino light curve and the energy spectrum of, ideally, more than one flavour. For the GW signal, a time-frequency analysis via spectrograms turns out to be a powerful tool which might reveal details about, e.g., oscillations in the PNS. Reconstructing the dynamics from future detections of this kind, however, is an intricate procedure and requires a detailed understanding of the physics.

The thermal production of large neutrino fluxes does not start with core collapse. During the last phases of nuclear burning, massive stars cool predominantly via neutrinos rather than photons [3410]. Hence, detecting the characteristic increase in neutrino emission as the star evolves though its last burning stages would provide a useful early warning months before collapse ensues [3411]. However, given the luminosities and the relatively low (sub-MeV) neutrino energies, it would only be feasible for nearby stars. At this stage, the compactness of the star and the, e.g., convective, velocities are too low for any detectable GWs to be produced.

For the subsequent core collapse and explosion itself (addressed in general in section 8.2.2), figure 148 shows the evolution of the luminosities and the mean energies of neutrinos observed at infinity obtained using a spherically symmetric simulation [3119]. The different phases indicated in the panels will be outlined in the following.

As the density and temperature of the core increase during collapse, the neutrino emission rises, in particular via the electron-capture process $e^- + p^+ \to n + \nu_e$. The rise is briefly interrupted when the core becomes optically thick at a central density $\rho_{\rm c} \sim 10^{12}\,{\rm gcm}^{-3}$. From this moment on, the properties of the emitted neutrinos are set to large degree by the conditions at the newly developed neutrinospheres [3412]. The collapse proceeds further until the PNS is formed. The outward moving shock wave releases a large fraction of the trapped neutrinos in the intense deleptonisation burst in which the luminosity of ν_e exceeds for a few ms values $L_{\nu_e} \gtrsim 3 \times 10^{53}\,{\rm erg/s}$. This very distinctive electron neutrino burst occurs in all stellar core collapse events. Its detection would serve as a very clear indication of the moment of bounce [3413]. As the height of the burst varies only slightly between stars, the count rates in a detector could furthermore be used to estimate the distance to the event.

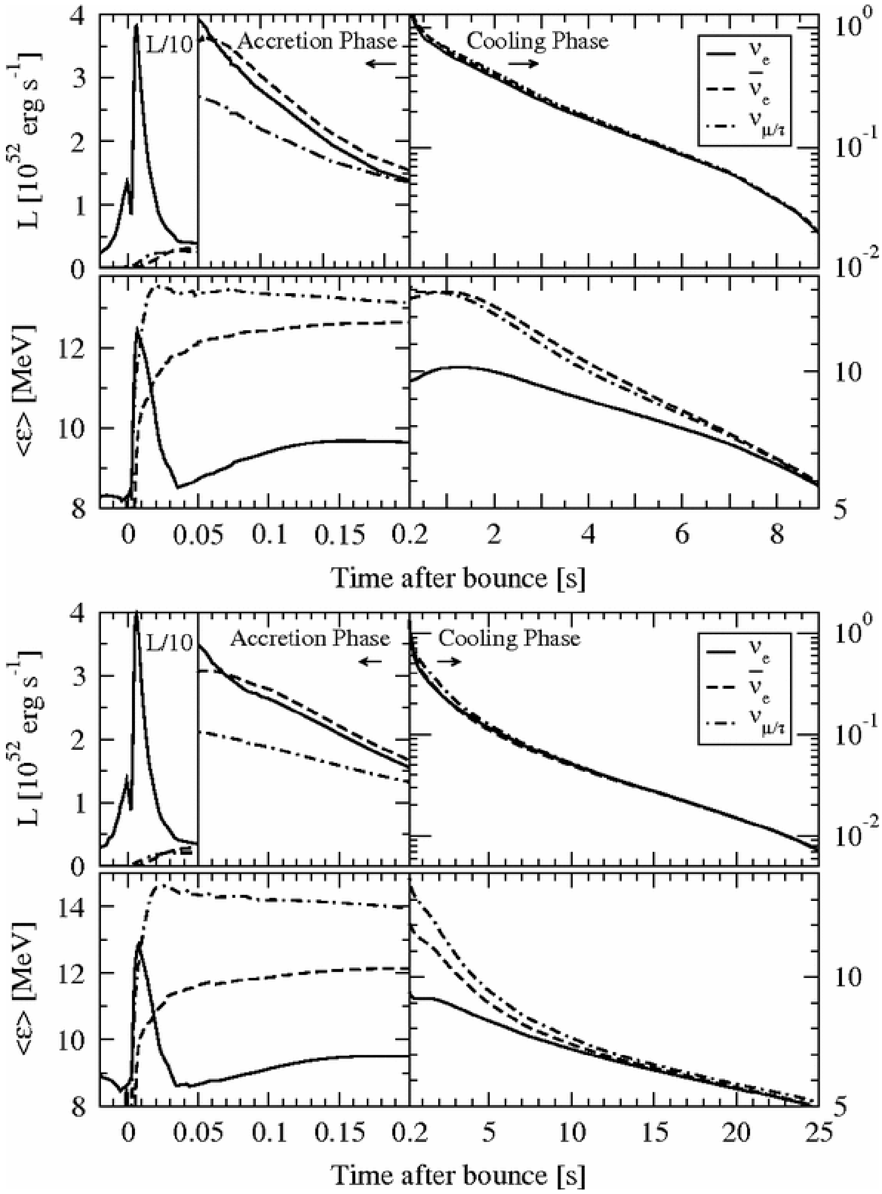

Figure 148. Time evolution of neutrino luminosities L and mean energies $\langle\varepsilon\rangle$ for a typical long-time simulation. Reprinted figure with permission from [3119], Copyright (2010) by the American Physical Society.

The collapse is mostly spherical and by itself does not generate any significant GWs. It can, however, amplify pre-existing asphericities caused, e.g., by rapid rotation of the core. In that case, the ensuing rapid anisotropic acceleration of the gas at bounce, followed by the decaying oscillations as the PNS settles into its new quasi-equilibrium, produces a signal composed of a short (few ms), large spike, and a series of lower-amplitude oscillations thereafter. The amplitude of the spike and the frequencies at which it is emitted can be used as probes for the rotational energy of the core as shown, e.g., in ref. [3414].

While L_{ν_e} declines after the burst, the production of the other flavours increases such that, after a few tens of ms, all flavours are emitted at roughly similar rates. Their spectra

JCAP03(2026)081

are approximately, though not exactly, thermal [3415–3417], with mean energies close to the gas temperature at the neutrinospheres. The ordering of the neutrinosphere radii, $R_{\mathrm{ns},\nu_e} > R_{\mathrm{ns},\bar{\nu}_e} > R_{\mathrm{ns},\nu_{\mu,\tau}}$, reflects the hierarchy of neutrino-matter interaction rates from strongest to weakest coupling and translates into an inverse order of the mean energies $\bar{e}_{\nu_e} < \bar{e}_{\bar{\nu}_e} < \bar{e}_{\nu_{\mu,\tau}}$.

Two main sources feed the neutrino emission: the thermal energy of the hot PNS and the accretion of matter falling toward it [3218, 3418]. The former leads to a luminosity that is similar for all flavours and decays on the Kelvin-Helmholtz timescale of the PNS, typically several seconds [3419]. The total energy emitted until the transformation of the PNS into a cold NS should approximately correspond to the total gravitational binding energy. That, in turn, is, for a given nuclear EOS, a function of the NS mass. Hence, observing the neutrino emission for a sufficiently long time could provide an estimate of the mass of the newly born NS. The cooling PNS emits all flavours at similar rates.

Matter keeps falling onto the PNS at least until an explosion sets in, and, in the case of very asymmetric explosions, potentially for much longer. The gravitational binding energy released in the process powers the second main component of the neutrino luminosity, which thus is a possible probe for the instantaneous accretion rate. It occurs mostly near the PNS surface where the matter settles into equilibrium. In the corresponding lower density range, $\nu_{\mu,tau}$ couple too weakly to matter to be emitted at significant rates. Consequently, accretion contributes mainly to the emission of ν_e and $\bar{\nu}_e$ [3218]. A pronounced drop in the luminosities of these flavours would thus be signature of the end of mass accretion, signalling in many cases a successful explosion.

Besides these long-term trends, the neutrino luminosities can show fluctuations on a range of time scales down to a few milliseconds. Additionally, the nonspherical geometry of the core leads to significant variations with emission directions. Given sufficiently high count rates, the former can be discovered in a detector equipped with a sufficiently fast readout system and with the help of time-frequency analysis techniques. The latter is harder to observe as any detector is limited to a single line of sight.

The SASI, which is only excited before the explosion sets in while the shock stalls at a low radius, leaves an imprint in the form of a modulation of the emission at frequencies around $\mathcal{O}(100)$ Hz [3134, 3420–3423]. An eventual detection could offer a way to infer the radius of the shock wave via its influence on the period of SASI spiral waves or sloshing motions. Additional variations at lower frequencies can come from the dynamics of the convection in the gain layer.

The neutrino emission is never perfectly spherical, but usually develops a large-scale anisotropy, in particular after the explosion is launched. Aside from this effect, three-dimensional simulations have revealed a large-scale asymmetry in the emission of ν_e and $\bar{\nu}_e$, the lepton number emission self-sustained asymmetry (LESA, [3354, 3424–3426]). It consists of a dipolar pattern in which the emission in one direction is dominated by ν_e and in the opposite direction, by $\bar{\nu}_e$. This geometry corresponds to a similar dipolar anisotropy of the electron fraction in the PNS. The dipole direction is random, but changes only slowly in time.

Further variations of the neutrino luminosities and mean energies can be observed if the rotation of the core periodically moves hotter and cold spots on the neutrinospheres across the line of sight. Furthermore, rapid rotation can cause a flattening of the core. The PNS and with it the neutrinospheres are situated at lower radii along the rotational axis than in the equatorial plane. As a consequence, the polar neutrino fluxes can be enhanced with respect to those at equatorial directions by several tens of percent.

Potential post-bounce episodes in which gravitational binding energy is released on short times are reflected in bursts of the neutrino emission [3099, 3427]. They can occur if the contraction of the core leads to a regime in which phase transitions of the nuclear matter change the adiabatic index of the EOS and, thus, cause the PNS to rapidly settle into a new quasi-equilibrium. These bursts tend to be lower and slower than the deleptonisation burst. Futhermore, they would not be visible in all flavours, not only the ν_e. If the PNS accretes enough mass for collapse to a BH to be inevitable, a similar rise of the neutrino emission occurs [3218]. In this case, however, it is followed by a very rapid dimming marking the moment of BH formation.

We note that most results on the neutrino emission are based on models that take into account neutrino emissions in a simplified manner at best. Thus, they may miss an important ingredient in the dynamics and the emission of the core itself as well as the propagation of the neutrinos to the detector. Collective oscillations could, e.g., swap neutrino flavors among each other, thus complicating the interpretation of a detection. The physical input such as neutrino masses and mixing angles required for describing the oscillations are still uncertain, and numerical methods adequate for long-term, large-scale simulations are under development [3428–3433].

Although at first sight the GW signal from CCSN may seem completely stochastic, in reality is rich in different features that carry information about the emitting object, mainly the nascent PNS. The main burst has a typical duration of ~ 1 s, starting at the core bounce. A number of numerical simulations have been performed focused in the analysis of the GW signal for the case of non-rotating progenitors both in 2D [3134, 3140, 3141, 3434–3438] and 3D [3069, 3080, 3148, 3375, 3439–3441]. For the case of rotating progenitors there is also extensive work by means of 2D [3072, 3140, 3442] and 3D simulations [3084, 3151, 3443–3445]. The different features present in the signal are described next:

Bounce signal: If rotation is present, the collapsing core is not perfectly spherically symmetric but deformed by rotation. The rotationally-induced quadrupolar deformation has its maximum time variation at the time of bounce, which produces a characteristic signal in coincidence with the bounce followed by a few oscillations in a timescale of a few ms (see figure 149). The dependence of the waveform on the rotation rate, the rotational profile, the equation of state and the progenitor mass has been extensively studied by [3414, 3446, 3447]. Numerical simulations show that the signal only has plus polarization and is characterized by its amplitude Δh (at a given source distance) and its peak frequency, related to the post-bounce oscillations. [3414] found that Δh is proportional to the ratio of rotational-kinetic energy to potential energy $T/|W|$. This relation breaks for sufficiently large rotation rates, $T/|W| > 0.06$, due to the effect of centrifugal forces in the dynamics, reaching a maximum value of about 3×10^{-20} at 10 kpc. In the same regimen, they found that the peak frequency, which is in the range $100 - 1000\,$Hz, scales with the square root of the mean density in the PNS. This dependencies open the possibility of measuring the rotation rate and putting

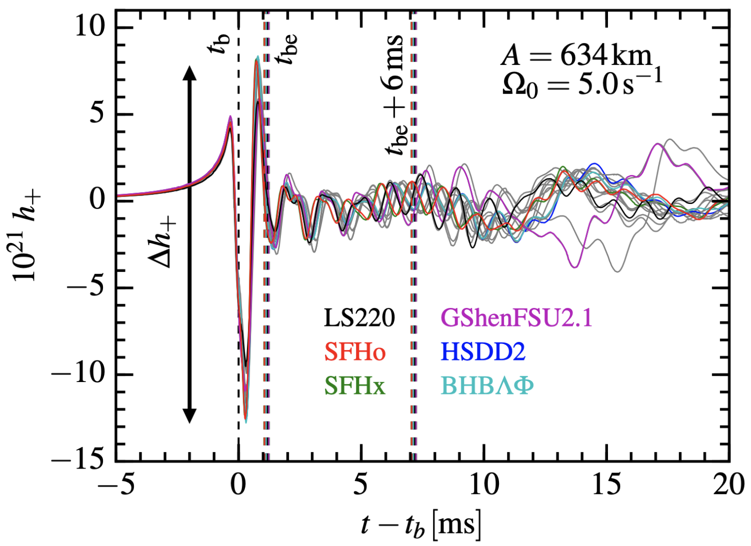

Figure 149. *Bounce GW signal*: strain during the first few ms of the collapse of a fast rotating progenitor computed for different EOS. The signal is cheracterized by the peak to peak amplitude, Δh_+, and the frequency f_{peak} of the post bounce oscillations up to ~ 6 ms. Reprinted figure with permission from [3414], Copyright (2017) by the American Physical Society.

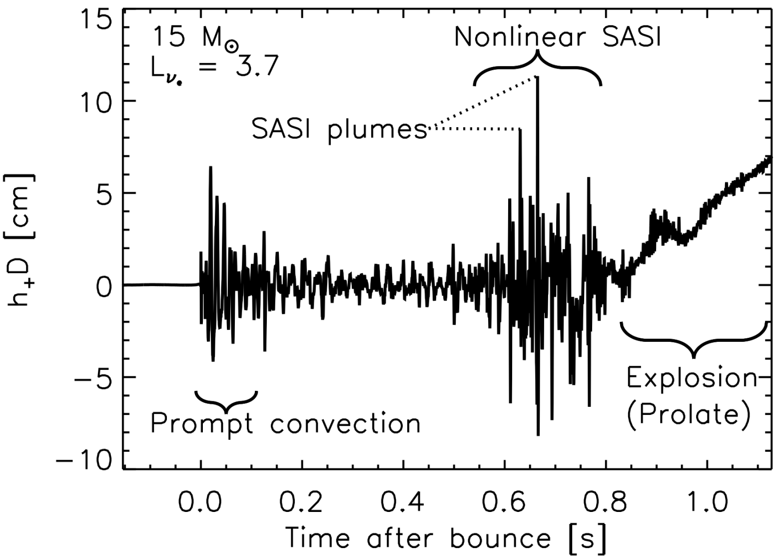

Figure 150. Typical strain during neutrino-driven SNe showing the different features present. Reproduced from [3434]. © 2009. The American Astronomical Society. All rights reserved.

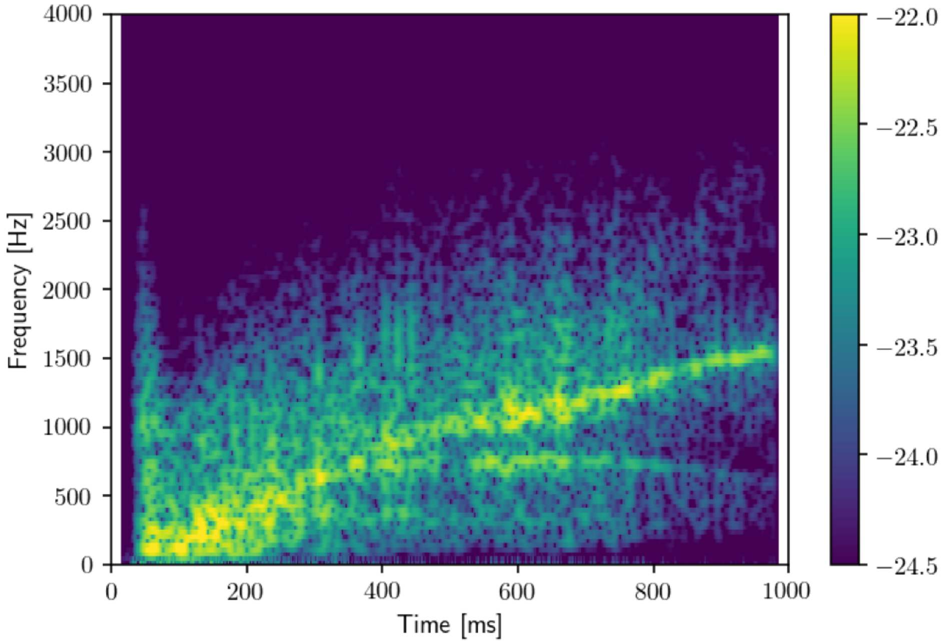

Figure 151. Spectrogram of a typical core-collapse simulation showing the tracks of different oscillation modes of the PNS. Reproduced with permission from [3075].

constrains on the EOS. Unfortunately, this feature is only present for fast rotating progenitors that are expected to be only a small fraction of all collapse events.

Prompt convection: About 10 ms after bounce symmetry of the PNS breaks due to the development of convection. In some cases the conditions in the PNS after bounce can trigger a strong episode of convection that produces a GW signature lasting for at most ~ 50 ms [3434, 3436, 3448] (see figure 150). Typical frequencies are $100 - 200\,\mathrm{Hz}$ and the strain amplitude is about 10^{-22} at 10 kpc. In case it is present, this phase can be followed by a quiescent phase, with lower GW amplitude, lasting for, at most, 200 ms.

PNS oscillations: The dominant GW emission mechanism in neutrino-driven supernovae are PNS oscillations sustained by the instabilities developing at the PNS region [3072, 3434, 3435], which are observed generically in all numerical simulations. The dominant component of the signal (the so-called ramp-up mode) is particularly easy to identify in the spectrogram of the GW signal where it appears as an arch with increasing frequency starting at about $100 - 500\,\mathrm{Hz}$ after bounce and raising to $500 - 2500\,\mathrm{Hz}$ after 0.6 s (see figure 151). Most of the energy of the signal is emitted in the first $0.2 - 1$ s after bounce, with a strain amplitude in the range $\sim 10^{-23} - 10^{-22}$ for non rotating progenitors. For rotating progenitors the strain increases with rotation up to values as high as $\sim 10^{-21}$ for a source located at 10 kpc. By comparing to the oscillation modes of the PNS, computed by solving the eigenvalue problem associated to a spherical background, it has been shown that this dominant component of the signal is the result of the excitation of a particular oscillation mode of the PNS [3074, 3075, 3141, 3449–3451]. The nature of this mode is unclear and has been proposed to be a g-mode [3072, 3074, 3075, 3088, 3435], a f-mode [3141, 3449, 3450, 3452] or some combination of both [3069]. The frequency of the dominant mode depends on the properties

JCAP03(2026)081

of the PNS at each time. Have been proposed universal relations, independent of the EOS or the progenitor model used, relating this frequency with the surface gravity (M/R^2), the mean density ($\sqrt{M/R^3}$) and the compactness (M/R) of the PNS [3077, 3088, 3453, 3454]. These relations allow developing GW asteroseimology by measuring the PNS properties from the frequency evolution of the dominant mode in the GW spectrogram. The development of this kind of relations for the case with rotation is something important to consider for the future.

Additionally, some simulations show a power gap in the spectrograms at about $1000-1300$ Hz [3069, 3087, 3140, 3141, 3375, 3455], breaking the dominant component in two. This gap has been attributed either to an avoided crossing between g and p-modes [3069, 3141] or to a minimum of the eigenfunctions of the PNS oscillation modes [3455]. [3090] have proposed the possibility of using the exact location of this gap to constraint the EOS of dense matter.

Apart from the dominant component there are some weaker modes excited that could observable and linked to the properties of the PNS.

- *SASI* induces a periodic signal (see figure 151) that can be also seen inf GW spectrograms [3072, 3434, 3435, 3448]. Although there is some basic understanding of the SASI through mode analysis (e.g. [3390]), detailed calculations based of simulations are still missing. If we use p-modes as a proxy for SASI modes (they behave similarly and share properties) one can conclude that the frequency of these modes could be used to determine the shock radius [3088].

- A *g-mode with decreasing frequency* [3088, 3089, 3140, 3141, 3455, 3456] has been identified starting at ~ 0.3 s post-bounce at a frequency of $\sim 600-800$ Hz that decreases with time to values as low as 200 Hz. This mode has been proposed to be a g-mode of the PNS core and its frequency seems to be highly sensitive to the EOS [3089, 3456].

- For fast rotating models, the *quasi-radial mode* contribute to the GW emission [3072]. The frequency of this mode goes to zero if the NS becomes unstable to collapse, therefore it can be used to infer the formation of a BH [3072, 3075].

Long-term PNS convection: even in the case of a successful explosion, the cooling PNS is still convectively unstable for timescales of $10-50$ s. This convection can produce a weak ($< 10^{-24}$) broad-band signal in the range $100-1000$ Hz [3457]. If fast rotation is present inertial modes can develop, with frequencies scaling with the rotational frequency of the PNS. The detection of these inertial modes is an interesting oportunity for asteroseismology. However, this signal can be suppressed if a strong dynamo is developed, case in which a low frequency signal (< 100 Hz) may apear instead.

Triaxial instabilities: a sufficiently fast rotating PNS can develop triaxial instabilities, typically a bar, that breaks axisymmetry and induces a strong GW emission with a frequency related to the rotation of the bar. The presence of differential rotation lowers the threshold of the instability allowing for the formation of bars a moderate rotation ($T/|W| > 0.01$). This is the so called Low-$T/|W|$ instability and has been observed in a number of simulations [3149, 3151, 3443, 3445, 3458–3460]. It leaves a very characteristic periodic oscillation with increasing frequency in the range $400 - 1000\,\text{Hz}$ and a strain amplitude up to about 10^{-21}. Once formed it is unclear how long this bars can survive since it could be destroyed by the presence of turbulent viscosity, driven by the presence of magnetorotational instabilities. In any case, this feature is only present for fast-rotating progenitors which are likely a small subset of all collapsing cores.

Memory: the asymmetric expansion of the exploding shock and anisotropic neutrino emission produces a low-frequency ($1 - 10\,\text{Hz}$) component of the GW signal [3434, 3436, 3448, 3461] that carries information about global asymmetries of the system (see figure 151).
Finally, we discuss other parameters that have an impact on the GW signal:

- The main impact of the *progenitor star* is through the structure of the iron core at the time of collapse, although for most stars the GW signal is qualitatively similar. Even for some extreme progenitors such that ultra-stripped helium stars, with masses as low as $3.5M_\odot$, produce GW signals comparable to other SN cases [3439]. Special mention require the case of low mass progenitors ($9 - 10M_\odot$) which explode easily and produce very short GW bursts of $0.1 - 0.35$ s (e.g. [3148, 3440]).
- *Black hole formation:* The signal is qualitatively similar for the case of successfully and failed explosions because the typical timescale in which the explosion develops is comparable or longer than the GW emission (see e.g. [3072]). The ring-down of the forming BH is expected to leave a very short (~ 0.1 ms) GW burst with a frequency of $\sim 5\,\text{kHz}$ [3462].
- The consideration of EOS with *QCD phase transitions* [3097, 3463, 3464] may leave an imprint in the GW signal, namely a secondary GW short burst (a few ms) at late times with strain amplitude ~ 10 times the main burst and frequencies in excess of $1\,\text{kHz}$

8.2.4 Observations: state of the art

Although most SNe probably are not strong sources of GWs, some cases, such as rapidly rotating hypernovae associated with Long Gamma Ray Bursts (LGRBs), magnetar progenitors or asymmetric CCSNe, are. Furthermore, the existence in binary systems of compact objects such as NS and BH, whose merger has been detected by GWs, implies that core-collapse supernovae have occurred before.

The characteristics of a SN, including its outcome, rest upon several factors, notably the evolutionary stage of the star that acts as the SN progenitor at the moment of its explosion, as well as its chemical composition and, possibly, its angular momentum [3465] (see also section 8.2.1). The observational heterogeneity observed in supernovae introduces a significant challenge in making precise theoretical predictions regarding the expected outcomes.

In the initial fundamental classification of CCSNe, we already distinguish between Type II SNe (SNII), which exhibit the residual hydrogen from the stellar envelope, and Type Ib SNe (SNIb, He-rich) or Type Ic SNe (SNIc, He-poor), characterized by the absence of hydrogen (e.g. [3466]). SNIIe are classified into two photometric subclasses based on their light curves: those displaying prominent plateaus (SNII-P) and those with linearly declining curves (SNII-L). Nowadays, the gap between the two classes has been filled with a continuous distribution of SNe with different light-curve slopes (e.g. [3467]). Additionally, two other main CCSN subclasses are recognised according to their spectra. The interacting SNe which are any SN type (it includes the core-collapse subfamilies IIn, Ibn, Icn) with fast ejecta and sufficient energy to interact with a slower and denser circumstellar material (CSM; [3468]), and the Type IIb SNe (SNIIb), whose spectra metamorphose in the following week from hydrogen-rich to helium-dominated, similar to those of the SNIb ([3469]). Since then, numerous additional SN groups have been identified, some of which we will discuss below.

Together the SNII-P and SNII-L represent the majority of CCSNe (considering a volume-limited rate in the local Universe; [3092]). Almost 9% is formed by interacting SNe. Instead, the intermediate grouping of SNIIb and the H-poor SNe (SNIb, SNIc) constitute the remaining $\sim 37\%$. [3470] find similar rates for CCSN groups considering a redshift range $0.15 < z < 0.35$ (see also section 8.2.5).

The large observational heterogeneity present in the SNe is closely related to the progenitor star's evolutionary state at the moment of the explosion. Here, a key parameter to predict the final fate of star evolution is the initial mass. Several indirect techniques to probe the progenitor have been utilized over the years, but the most straightforward method involves pinpointing the star that underwent an explosion. The search for such progenitors demands precise spatial resolution and accurate astrometry in both pre- and post-SN explosion images. Source confusion in densely populated environments poses a significant challenge, especially for more distant objects. Therefore, the majority of these identifications have been achieved by examining archival images captured by the Hubble Space Telescope (HST; e.g. [3471]) and recently by the James Webb Space Telescope (JWST; e.g. [3472]) before the explosion occurred.

In recent years, it has derived a limited range from 8 to 17 $M_\odot$ for the progenitor mass of SNe H-rich. As theoretically expected (see section 8.2.1) these seem to have exploded in the red supergiant phase. However, other surprising cases of massive stars exploding unexpectedly as yellow hypergiants (e.g. [3473, 3474]) or luminous blue variables [3475, 3476] have been observed. Furthermore, evidence for enhanced mass loss on timescales of years to days before a star undergoes core collapse [3477], as well as stars exploding within shells of circumstellar dust [3478] has been accumalated.

A well-known case of H-rich SN whose progenitor was not found to be a RSG is the peculiar SNII-P SN 1987A in the Large Magellanic Cloud. Sk -69° 202, a blue B3I supergiant star, was identified at the SN position on pre-SN ground-based images ([3479–3481]), with a mass of ~ 20 $M_\odot$ ([3482, 3483]). SN 1987A is the SN know well as the first example of a multi-messenger event observed through neutrinos and photons. This SN showed a light curve that did not resemble any of those observed up to that moment, challenging many of the scientific models of the time. It showed that its explosion was not as symmetric as previously thought ([3484, 3485]). It was also possible to analyse the dust released by a SN (e.g., [3486–3490] and detect for the first time neutrinos created just when the core of the massive star exploded as a SN (see, e.g., [3491]). The latest discovery provided by SN 1987A came recently with observations from the ALMA radio interferometer and JWST, confirming that in the central parts of the SN remnant, there is a cloud of dust that is very hot and brighter than its surroundings. This discovery suggests that the explosion remnant was a NS currently hidden within the dust cloud ([3492–3494]).

JCAP03(2026)081

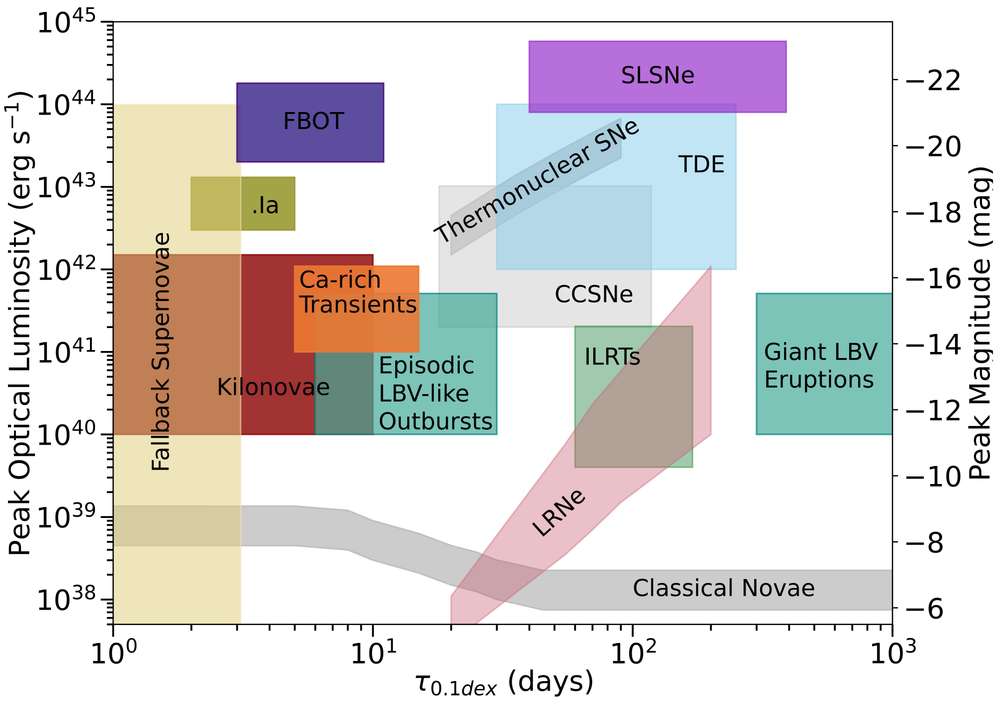

Figure 152. Relationship between peak optical luminosity and characteristic time (defined as the duration for a luminosity decline of 0.1 dex) for optical transients within the local Universe. Different regions, denoted by various colours and shapes, indicate the typical location of some representative classes of transients such as SuperLuminous Supernovae (SLSNe), Tidal Disruption Events (TDEs), CCSNe, Luminous Blue Variables (LBVs), Intermediate Luminosity Red Transients (ILRTs), Luminous Red Novae (LRNe), and others. Reproduced from [3503]. CC BY 4.0.

H-poor CCSNe could instead arise either from more massive single-progenitor stars than hydrogen-rich SN one ($\geq 20\ M_\odot$) or from lower mass stars $8M_\odot < M < 30M_\odot$ in a binary system [3495]. In binary systems, they are expected to be stripped of mass by their companion stars, however, this process alone is insufficient to completely remove the hydrogen envelope of a star and they must evolve into a helium giant phase to shed the remaining mass [3496]. The difficulty in detecting them is because these SNe tend to occur near complex, crowded environments (see, e.g. [3497]). Despite our best efforts and a bunch of upper limits [3496], there are only two tentative identifications of progenitor stars for SNIb (iPTF13bvn; e.g. [3498] and SN 2019yvr; [3499]), and a potentially hot and luminous candidate progenitor for a SNIc (SN 2017ein; [3500–3502]).

It is worth noting that both single-star and binary systems scenarios are used in the current search for CCSN progenitors since most massive stars ($\sim 70\%$) live in interacting multiple systems [1424]. From a different perspective, the abundance of binary systems implies that binary interaction plays a predominant role in the evolution of massive stars, giving rise to phenomena such as stellar mergers and gamma-ray bursts.

Since the initial SN classification, further SN types have been recognized (see figure 152), such as the Broad-Line Type Ic supernovae (SNIc-BL) linked to high-energy gamma-ray bursts (GRBs; [3504]) and the Super Luminous Supernovae (SLSN; [3505]).

SNIc-BL are a subclass of SNIc characterised by extreme velocity dispersion in their spectra at and before the peak ($\sim 19000\,\mathrm{km\ s^{-1}}$; [3506]), causing the spectral lines to appear broader than in other types of supernovae. They are often found in association with LGRBs and are then believed to be linked to the deaths of rapidly rotating massive stars, which can produce powerful jets of material and radiation (e.g. SN 1998bw, located in the error region of the GRB980425; [3507]). However, there are relativistic SNIc-BL without a detected GRB (e.g. SN 2009bb; [3508]). SNIc-BL similar to those associated with GRBs are intrinsically rare, being constrained its rate to ≤ 950 Gpc^{-3} yr^{-1} ([3509]).

The SLSNe can be hundreds of times brighter than SNe found over the last decades ($\mathrm{M}_V > -21$ mag), having an energetic not explained by the standard core-collapse and neutrino-driven mechanisms (see, e.g., [3510]). Since the first reported SLSN, SN 2005ap ([3511]), we have built a catalogue of approximately 100 such events, a number steadily growing thanks to ongoing sky surveys. This sample of events has allowed us to classify SLSNe into two main types based on the presence or absence of hydrogen in their spectra: SLSN-I and SLSN-II. While SLSNe are rare compared to more common SN types, with SLSN-II being less frequent than hydrogen-poor SLSNe, they are nonetheless significant cosmic phenomena. The volumetric rate of SLSNe, including both hydrogen-rich and hydrogen-poor events, is estimated to be between 0.4 and 1 event per several thousand supernovae (e.g., [3512]). Standard SN progenitors typically synthesize about $0.1\,M_\odot$ of ^{56}Ni, while SLSNe demand $\geq (1-10)M_\odot$ of this isotope (see, e.g. [3513, 3514]). Therefore, SLSNe seem to favor alternative explosion scenarios to the traditional SN energy sources of radioactive decays of ^{56}Ni and ^{56}Co. It is proposed that the additional energy is provided, for example, by a shock between the SN ejecta and CSM shed by the progenitor star before its explosion (see, e.g., [3515]) or by the radiation from a newly-formed, highly magnetized NS (a magnetar) deposited into the ejecta (see, e.g., [3515, 3516]). However, no models yet provide an excellent and unique interpretation of the observations.

The peak luminosities and radiant energies of SNIc-BL and SLSNe, which exceed those of typical supernovae by several orders of magnitude, lead to the hypothesis that the progenitor stars are more massive than typical CCSN progenitors (e.g., [3517, 3518]). The spectroscopic analysis, particularly during the nebular phase, and the study of their host galaxies suggest that SLSNe and SNIc-BL associated with long GRB might share similar progenitors and/or explosion mechanisms ([3510]). Although there is no direct observational evidence, magnetar-driven models which involve the energy injection from a rapidly spinning magnetar (see below and [3516, 3519]) successfully explain the observed light curves of both SN families (e.g., [3514, 3520–3523]). In addition, jets launched by the central engine in these events are widespread (e.g., [3524–3529]). The possible magnetar formed at the collapse of a massive star slows down quickly due to its magnetic field, sometimes causing it to emit focused jets that can punch through the star's outer layers. These jets can also provide enough energy to cause the star to explode as a SN. Furthermore, a jet will introduce asymmetries in the ejecta that may explain peculiar features also depending on the viewing angle. Indeed, SN observations suggest that many, if not most, CCSN explosions exhibit asymmetric features (e.g., [3530–3534]).

As previously described the more massive stars should end their lives as failed, or dark, SNe (see section 8.2.1). These events occur when, after the initial phase of the explosion, the

JCAP03(2026)081

mantle of the star collapses back onto the core and the consequence is the formation of a BH without the occurrence of a visible SN (e.g., [1743, 1758, 1759, 3535]). Models suggest that about $(10 - 30)\%$ of core collapses lead to failed SNe, supported by the lack of higher mass SN progenitors ([3139, 3536], but see [3537, 3538]). Some efforts have been made to identify failed SNe using telescopes to search for disappearing RSGs without an associated SN (e.g., [1754, 3536, 3539, 3540]). The first candidate discovered was N6946-BH1 [1754, 3541]. It was a red source consistent with a mass $(18 - 25)\, M_\odot$ RSG star, which disappeared after a long-duration weak transient. Later, ref. [1755] did not find any optical counterpart and only low-luminosity near-IR and no mid-IR counterparts compared to the estimated progenitor luminosity. Recently, [3542] have found a very red, dusty source at the candidate location in the mid-IR with data from the JWST. Overall, it has been estimated that failed SNsne occur at a rate of one every 300–1000 years (see, e.g., [3543]) in the Milky Way galaxy and its satellites. More recently, [3540] quantified the fraction of core collapses that fail to produce SNe at $0.16^{+0.23}_{-0.12}$ (at 90% confidence level).

Failed supernovae could theoretically produce GWs; however, these waves may be weak due to a lower level of asymmetry compared to more energetic supernovae and could have lower frequency emissions since the core collapse often leads directly to the formation of a black hole without significant shock waves or turbulence (e.g., see [3544] and [3072]). As a result, detecting these GWs is challenging for current observatories like LIGO and Virgo. However, third-generation detectors, such as the Einstein Telescope, may detect them.

8.2.5 Observed rates and expected rates in the local Universe

8.2.5.1 The observed CCSN rate in the local Universe. The history of SN discovery and the measurement of the SN rate is a fascinating evolution from serendipitous observations to systematic surveys. In the past, nearby SNe were all discovered serendipitously by amateurs and astronomers. The first significant organized effort to search for SN events was initiated by F. Zwicky in 1942 with the Schmidt telescope on Palomar. Zwicky was able to obtain the first estimate of the SN rate based on a small sample of 19 SN events. In 1964 Rosino began a systematic search for SNe at Asiago Observatory discovering 30 SNe. Since Zwicky and Rosino pioneering efforts there have been numerous attempts to estimate the local SN rate. However, it was not until the 1980s and early 1990s that the measurement of the local SN rate became more accurate. During this period, the sample size of observed SNe grew substantially, and improvements in observational techniques allowed astronomers to make more precise estimates [3545, 3546]. ref. [3545] combined data of five optical surveys in the nearby Universe using wide-field telescopes and photographic plates, collecting 67 CCSNe in a reference sample of about 10000 galaxies. More recently, the Lick Observatory Supernova Search (LOSS) at the Katzman Automatic Imaging Telescope equipped with a digital camera measured the rate for each SN type monitoring a sample of 14882 galaxies up to $z \leq 0.035$ and discovering 106 CCSNe within 60 Mpc and 440 CCSNe in the overall galaxy sample [3547].

The landscape of optical transient searches is changed considerably in the last decade with the advent of wide-field all-sky surveys (e.g. Catalina Real-Time Survey, Palomar Transient Factory, Rapid Response System-Pan-STARRS, All Sky Automated Survey for SuperNovae) monitoring the local Universe with a regular cadence and a deeper limiting

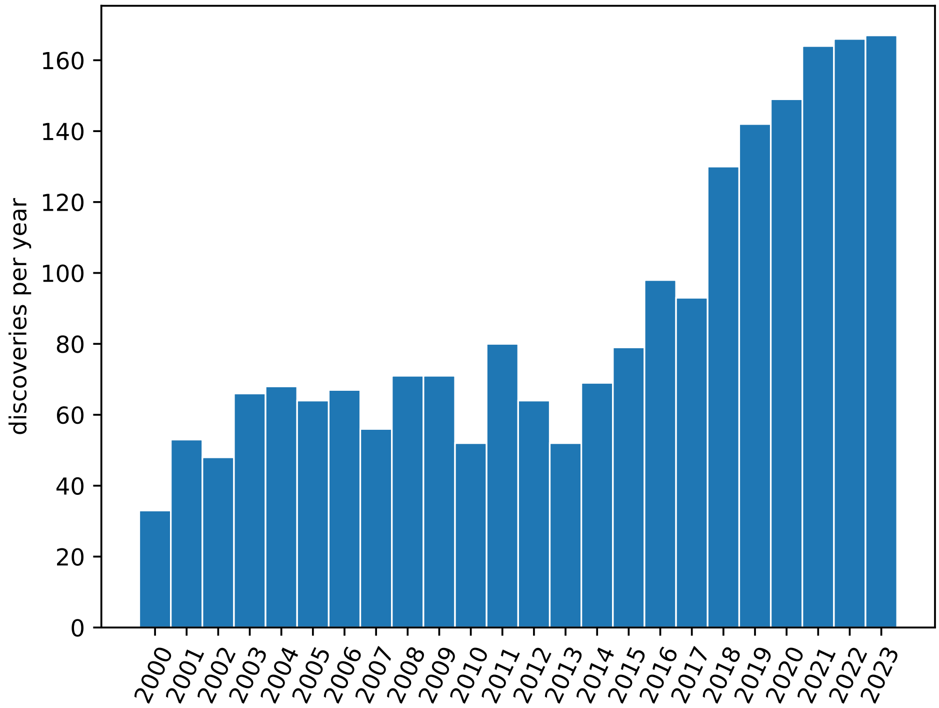

Figure 153. The yearly distribution of CCSNe with spectroscopic classification from 2000 to 2023 within 100 Mpc.

magnitude compared to past searches. The significant increase in the number of SN discoveries over the past decade, driven by new SN surveys (as shown in figure 153), is revealing a remarkable diversity in SN types. This progress has enabled the discovery of new classes of stellar explosions as such as SLSNe and Intermediate Luminosity Optical Transients (ILOTs) (see section 8.2.4).

In particular, from 2017 the Zwicky Transient Facility (ZTF) [3548] at 48 inch Samuel Oschin Telescope (Schmidt-type) at the Palomar Observatory scans the entire Northern sky every two days with a median single visit depth (5 sigma) of 20.4 mag in R band and the Asteroid Terrestrial impact Last Alert System (ATLAS) [3549] which consists of four telescopes (two in Hawaii, one in Chile, one in South Africa) automatically scans the whole sky several times every night with a median depth of 19.5 mag.

Assuming that modern SN searches are very close to guarantee a continuous full-sky monitoring and an almost complete census of SN explosions in the local Universe we can easier estimate the CCSN rate (CCSNR) counting the CCSNe reported in transient discovery repositories and archives (the Asiago SN catalogue,[65] Transient Name Server[66] and Bright SNe catalogue[67]).

We analysed the sample of transients discovered in different volumes of the Local Universe (within a radius of 10, 50 and 100 Mpc) in two time intervals, from 2000 to 2023 and from 2018 to 2023, the beginning of ZTF and ATLAS surveys. The number of CCSNe discovered

[65] http://sngroup.oapd.inaf.it [3550].
[66] https://www.wis-tns.org.
[67] https://www.rochesterastronomy.org/snimages.

	10 Mpc		50 Mpc		100 Mpc	
	SFR ($M_\odot$ yr^{-1})	CCSNR (yr^{-1})	SFR ($M_\odot$ yr^{-1})	CCSNR (yr^{-1})	SFR ($M_\odot$ yr^{-1})	CCSNR (yr^{-1})
LOSS		0.3±0.04		37.0±6		295±46
Kennicutt et al.	87±4	0.40±0.02				
Lee et al.	123±8	0.6±0.04				
Bothwell et al.	75±5	0.4±0.02	9420±602	45±3	75360±4814	362±23
Hopkins & Beacom	65	0.3	8836	42	76121	365
Madau & Dickinson	63	0.3	8059	39	66568	319
Observations		$1.1^{+1.7}_{-0.6}$		38.0±3		153±5

Table 14. Our estimates of the expected CCSNe per year within 10 Mpc, 50 Mpc and 100 Mpc, respectively. These estimates are derived from the volumetric rate measured by LOSS, several measurements of the total SFR in the same volumes, and our estimates of the observed number of CCSNe per year based on discovery reports and archives.

from 2000 to 2023 is 27, 680 and 2030 within 10, 50 and 100 Mpc, respectively, yielding rates of $1^{+1.7}_{-0.6}$, 28±1, and 85±2 events per year. If we consider the temporal range from 2018 to 2023, we found 229, and 916 CCSNe detected within 50, and 100 Mpc, respectively, corresponding to rates of 38±3, and 153 ± 5 events per year. The results of our analysis are presented in table 14. We emphasize that the observed number of CCSNe provides a stringent lower limit on the intrinsic number of CCSNe exploded in each volume.

The incompleteness of CCSN sample collected from archives arises from several factors: the effective search area in the sky, the fraction of intrinsically faint CCSNe that are missed by local SNe surveys due to their limiting magnitude, the fraction of CCSNe obscured by dust that remain undetected by optical searches, and the fraction of transients lacking classification.

To estimate the fraction of faint CCSNe missed by modern surveys, we assumed an average limiting magnitude of 20 mag for the SN searches which corresponds to absolute magnitudes of −10 mag, −13 mag, and −15 mag, at distances of 10, 50 and 100 Mpc, respectively. The cumulative luminosity function of CCSNe measured by LOSS survey [3092] indicates that approximately 20% of CCSNe are fainter than −15 mag and about 5% of CCSNe are fainter than −13 mag. We expect that local SN searches are nearly complete within 50 Mpc, but miss about 20% of CCSNe that explode within 100 Mpc.

The number of nearby CCSNe missed due to dust extinction remains largely uncertain. Dust extinction can significantly reduce the number of detectable SNe, especially in starburst galaxies, where the dust content is higher than in normal galaxies.

SN searches in near-IR wavelength range using adaptive optics have yielded a number of SNe in nuclear region of the Ultra Luminous InfraRed Galaxies (ULIRGs) with a broad range of host galaxy extinctions (for more details, see [3551]). ref. [3552] monitored 46 LIRG at near infrared wavelengths to search for obscured SNe, and detected only about $(10-30)$% of the expected SNe for far infrared luminosity of the galaxies. Ref. [3553], following the approach of [3552] and exploiting high resolution adaptive optics, found that the fraction of SNe missed due to high dust extinction has an average local value of approximately 20%. Results from the Spitzer InfraRed Intensive Transients Survey (SPIRITS) which monitored a large number of very nearby ($< 35\,\mathrm{Mpc}$) galaxies between 2014 and 2018 suggest that the fraction of CCSNe in nearby galaxies missed by optical surveys could be as high as 38.5% [3554]. More recently, ref. [3555] performed a systematic search at $3.6\,\mu$m for dust-extinguished SNe in the nuclear regions of forty LIRGs within 200 Mpc, resulting in the detection of 5 SNe that had not been discovered by optical searches. However, the spatial resolution of Spitzer was not optimal for searching for obscured SNe within the nuclear regions of ULIRGs. In contrast, high-resolution ground-based radio surveys have successfully discovered nuclear SNe with rates consistent with the galaxy IR luminosities. Nevertheless, not all SNe are sufficiently bright at radio wavelengths to allow a complete survey with the radio telescopes currently available to us [3556].

We also estimated the fraction of transients without spectroscopic classifications and found an average value of 35% within both 50 and 100 Mpc. A portion of these transients are likely CCSNe but accurately determining their number remains challenging.

By combining the fraction of faint CCSNe, dust obscured CCSNe and CCSNe without a spectroscopic classification, we infer that about 40% of the CCSNe exploded within 100 Mpc remain undetected.

Our estimate of the observed number of CCSNe in each volume can be compared with the expected number based on the CCSNR measured by the systematic SN search LOSS. The CCSNR measurements from LOSS have been normalised per unit B and K band luminosity, and their conversion into a volumetric rate requires knowledge of the local luminosity density for galaxies of different Hubble types. ref. [3092], adopting the following luminosity densities for early type and late type galaxies from [3557],

$$j_{\text{early type}} = (2.25 \pm 0.36) \times 10^8\, L_\odot \mathrm{Mpc}^{-3}\,, \tag{8.1}$$

$$j_{\text{late type}} = (2.96 \pm 0.42) \times 10^8\, L_\odot \mathrm{Mpc}^{-3}\,, \tag{8.2}$$

obtained a volumetric rate of $0.258 \pm 0.044 \times 10^{-4}\,\mathrm{Mpc}^{-3}\mathrm{yr}^{-1}$ for SN Ib/c, and of $0.447 \pm 0.068 \times 10^{-4}\,\mathrm{Mpc}^{-3}\mathrm{yr}^{-1}$ for SNII. The total CCSNR ($0.7 \pm 0.11 \times 10^{-4}\ \mathrm{Mpc}^{-3}\mathrm{yr}^{-1}$), when multiplied by the volumes within 10 Mpc, 50 Mpc and 100 Mpc, gives 0.3 ± 0.04, 37 ± 6 and 295 ± 46 CCSNe per year, respectively.

Our estimate of the observed number of CCSNe per year within 10 Mpc is about a factor four higher than the expected value from the LOSS volumetric rate. The discrepancy can be explained by the observed galaxy overdensity within 10 Mpc [3558] which results in a higher luminosity density compared to that assumed in [3092] for estimating the volumetric CCSNR, as described by eqs. (8.3) and (8.4) below. The expected CCSN number from LOSS volumetric rate matches the observed CCSNe within 50 Mpc while is about a factor two higher within 100 Mpc.

8.2.5.2 The expected CCSN rate from SFR measurements. Due to the short lifetime of their progenitor stars, the CCSNR closely follows the current SFR in a stellar system, making it possible to infer the CCSNR in a galaxy sample by adopting a progenitor scenario and measuring the total SFR in the sample. If we assume that the time interval between the formation of the CCSN progenitors and their explosion (delay time) is negligible, and that the SFR remains constant during this period, we obtain a linear relation between CCSNR and the SFR $\psi(z)$,

$$\mathrm{CCSNR}(z) = K_{CC}\psi(z)\,. \tag{8.3}$$

Assuming that all stars with suitable masses ($m_l^{CC} - m_u^{CC}$) become CCSNe, the scale factor is given by:

$$K_{CC} = \frac{\int_{m_l^{CC}}^{m_u^{CC}} \phi(m)dm}{\int_{m_l}^{m_u} m\phi(m)dm} \tag{8.4}$$

where $\phi(m)$ is the initial mass function (IMF), and $m_l - m_u$ is the mass range for the IMF.

The estimate of K_{CC} requires knowledge of the presupernova evolution of massive stars and of their final fate and depends on: (1) the value of the minimum mass that explodes as a CCSN (M_{CCSN}); (2) the minimum mass that produces a failed (and therefore undetectable) SN M_{DC}; (3) the limiting masses that form the various types of Wolf-Rayet stars (M_{IIP}) (see section 8.2.1). Since we are focusing on the Local Universe we can, as a first approximation, assume the limiting masses for the solar metallicity reported in table 13 at the beginning of this section. Adopting a Salpeter IMF in the range $(0.1 - 100)\,M_\odot$ [1700] and a progenitor mass range of $(9 - 25)\,M_\odot$ for CCSNe, we obtained:

$$K_{CC} = 4.8 \times 10^{-3} M_\odot^{-1}\,. \tag{8.5}$$

The luminosity of a galaxy is a sensitive tracer of its stellar population, allowing a direct connection between luminosity and instantaneous SFR when the observed emission originates from short-lived stars or brief phases of stellar evolution. Measurements of the SFR in the local Universe are based on Hα, Far Ultraviolet (FUV) and Total Infrared (TIR) galaxy luminosities. The total SFR in a given volume can be estimated using two different approaches: summing the SFR of each galaxy within this volume or extrapolating at $z \sim 0$ a model of the cosmic Star Formation Density (SFD) based on measurements in a larger range of redshift.

The total SFR in a galaxy sample. We estimated the total SFR within a volume of radius 10 Mpc by summing the measurements based on Hα [3559], Ultraviolet (UV) and TIR luminosity [3560] for a sample of 398 nearby galaxies from the 11 Mpc Hα UV Galaxy Survey (11 HUGS) and Spitzer Local Volume Legacy programs [3559] as in [3561]. The total SFR based on $\mathrm{L}_{H\alpha}$ is lower than that obtained from L_{FUV} and TIR luminosities, likely due to the attenuation correction. A detailed analysis of these differences can be found in [3561] and in [3562].

By adopting the SFR based on $\mathrm{L}_{H\alpha}$, we found that the expected CCSN number within 10 Mpc is 0.4 events per year, whereas when adopting the SFR based on L_{FUV} and total IR luminosity, it is 0.6 events per year. For volumes with radii of 50 Mpc and 100 Mpc, we used the SFR estimate in [3563], based on measurements from a large (> 10000) sample of galaxies selected from the Imperial IRAS Faint Source Catalogue Redshift Database (IIFSCz) catalogue, as well as the GALEX All-Sky Imaging Survey, augmented by the 11 HUGS dataset

JCAP03(2026)081

to include systems with low SFR, low metallicity and low dust content. This UV and IR dataset covers the full range of SFR behaviour, ensuring that both obscured and unobscured star formation are represented. It provides a SFD of $0.025 \pm 0.0016\, M_{\odot}\mathrm{yr}^{-1}$ Mpc^{-3} at $z \sim 0$. We used a scaling factor of 0.72 to adjust the SFD to our cosmological model yielding $(0.018 \pm 0.015)\, M_{\odot}\mathrm{yr}^{-1}\,\mathrm{Mpc}^{-3}$.

By adopting the SFR estimate from [3563], we derived the expected number of CCSNe as 0.4 ± 0.02 events per year within 10 Mpc, 45 ± 3 events within 50 Mpc, and 362 ± 23 events per year within 100 Mpc, as shown in table 14. The expected number of events within 10 Mpc is consistent with the value obtained by adopting the SFR measurements from [3559, 3560].

The cosmic SFD models. ref. [3564] mapped the evolution of the cosmic SFD by collecting FIR measurements from the Spitzer and UV measurements from the SDSS GALEX and the COMBO17 and Hubble Ultra Deep Field project and Hα derived measurement at low redshift. They performed parametric fits to the SFD using the form of ref. [3565],

$$\psi(z) = \frac{(a + bz)h}{1 + (z/c)^d}\; M_{\odot}\mathrm{yr}^{-1}\,\mathrm{Mpc}^{-3}\,. \tag{8.6}$$

The coefficients of the parametric form used in [3564] depend on the choice of the IMF and are $a = 0.017$, $b = 0.13$, $c = 3.3$ and $d = 5.3$ for a Salpeter IMF A with a high-mass power-law slope of 1.35 [3566]. We scaled these parameters to a Salpeter IMF using a factor of 0.77.

Madau & Dickinson (2014) [1587] based their modeling of the cosmic SFD evolution on a limited set of post-2006 galaxy surveys. This set includes only surveys that measured SFRs from rest-frame FUV or MIR and FIR data from Spitzer or Herschel. In some cases, this set also incorporates older measurements for local luminosity densities from IRAS or GALEX, as well as GALEX-based measurements at higher redshifts. They adopted a fitting function that is a double power law in $(1 + z)$ defined as:

$$\psi(z) = 0.015\frac{(1 + z)^{2.7}}{1 + [(1 + z)/2.9]^{5.6}}\; M_{\odot}\mathrm{yr}^{-1}\,\mathrm{Mpc}^{-3}\,. \tag{8.7}$$

We extrapolated both the parametric form from [3564] and from [1587] to $z \sim 0$ in order to estimate the expected CCSNR in the Local Universe.

We found that the expected number of CCSNe from SFD measurements is 0.3 events per year within 10 Mpc when adopting SFD values from both [3564] and [1587]. Within of 50 Mpc, we expect 42 and 39 CCSNe per year, corresponding to the SFD values from [3564] and [1587], respectively. And within 100 Mpc, the expected number of CCSNe is 365 and 319 events per year, respectively. These results are in good agreement with those obtained from SFD measurements in [3563]. See table 14 for a detailed summary.

8.2.5.3 Comparison between observed and expected CCSNe. The results of the comparison between the expected CCSN numbers from SFR measurements assuming a mass range of $(9 - 25)\, M_{\odot}$ for CCSN progenitors and the observed CCSN numbers for each volume we analysed are presented in table 14 and shown in figure 154.

Our estimate of the observed number of CCSNe within 10 Mpc is 2 to 3 times higher than our estimate of the expected number from the total SFR values by [3559] and [3560]. It

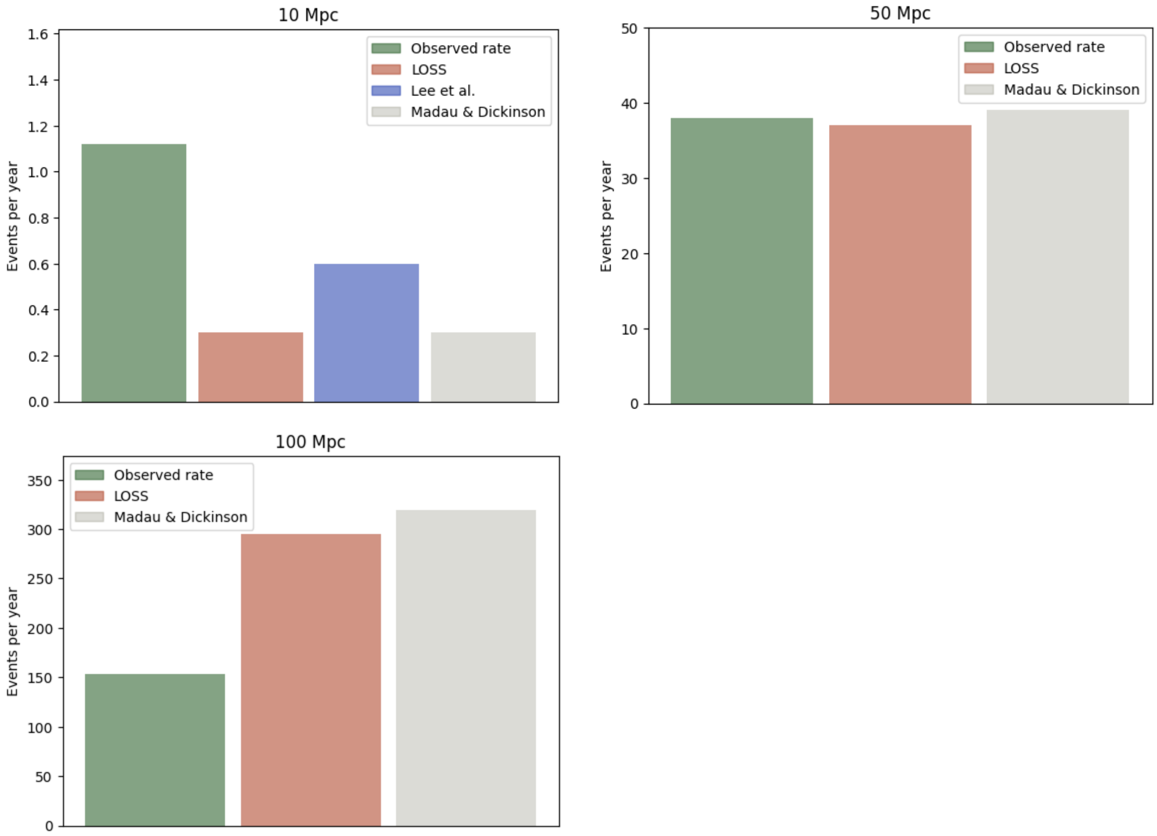

Figure 154. Comparison between the observed number of CCSNe and expected number obtained using different approaches within 10, 50 and 100 Mpc. For the expected CCSNR from the cosmic SFD, we adopted the parametric form from [1587] as a reference.

is important to note that all the host galaxies of CCSNe discovered within the last 24 years in this volume are included in the galaxy catalogues selected by [3559] and [3560]. ref. [3561], analysing the CCSNe discovered within 11 Mpc from 1998 to 2010, measured a CCSNR of $1.1^{+0.4}_{-0.3}$ events per year. By comparing this result with the expected CCSNR from 11 HUGS SFR measurements, they concluded that the measurements from L_α may under-estimate the total SFR by nearly a factor of two. Furthermore, our estimate of the observed number of CCSNe per year within 10 Mpc is about a factor four higher than our estimate of the expected number based on the extrapolation $z \sim 0$ SFD models, a discrepancy attributed to the observed galaxy over-density within 10 Mpc [3558].

The expected numbers of CCSNe from different SFD measurements [1587, 3563, 3564] are in good agreement with the observed number within 50 Mpc. However, they all exceed the observed rates by a factor of two within 100 Mpc.

These results are consistent with those obtained from the comparison with the expected values derived from CCSNR by LOSS survey.

8.2.5.4 Observed and expected CCSNR in the Milky Way. The estimate of CCSNR in the Milky Way (MW) is crucial for planning the observational strategy of current and next generation GW and neutrino detectors. Detecting a neutrino burst, a GW signal, shock

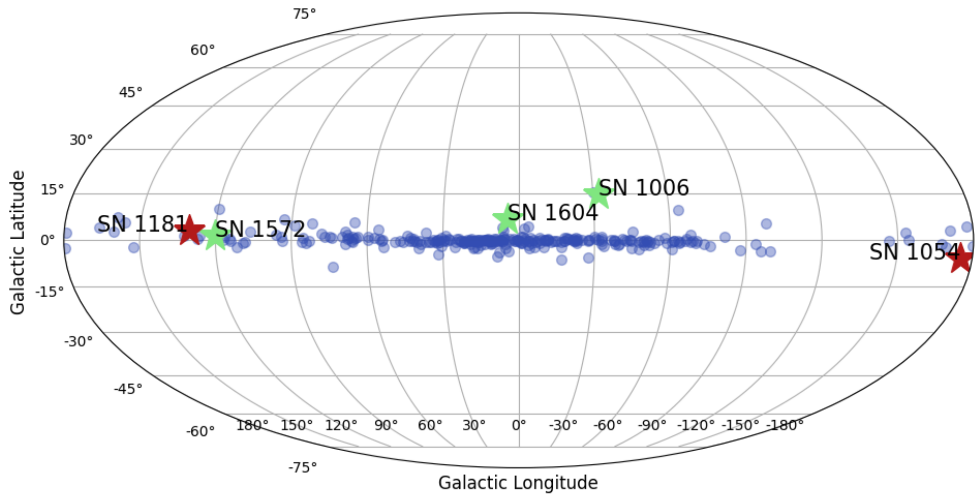

Figure 155. The distribution of the historical SNe and SN remnants in the galactic coordinate system is shown. CCSNe (SN1054 and SN1181) are showed as red stars, SNIa (SN1006,SN1572,SN1604) as green stars, and the SN remnants from the Green catalogue [3571] as blue dots.

breakout emission and gamma rays from a Galactic CCSN will provide direct and significant constraints on CCSN explosion mechanism. The most recent recorded SN explosion in our Galaxy occurred in 1604. However, the study of young SN remnants suggests that at least two SN events have occurred in the past 400 years in our Galaxy. The expansion age of the Cassiopeia A remnant (G111.7-2.1), approximately 325 yr, indicates that the SN explosion took place around AD 1681 $\pm$ 19 [3567]. Additionally, the most recently discovered SN remnant G1.9+0.3 has an age of $\sim 110-180$ years, making it the youngest-known remnant in our Galaxy with an explosion date placed in the second half of the 19$^{\text{th}}$ century [3568–3570]. A significant fraction of SN events in the MW remains undetected in the optical range due to heavy dust absorption in the Galactic disk. Despite advancements in observational capabilities across other wavelengths (e.g., radio telescopes), and the advent of neutrino and GW detectors, no other SNe have been discovered since SN1604. Different approaches can be adopted to infer the Galactic CCSNR based on both direct and indirect evidences:

- the number of historical records of SNe combined with spatial distribution models for Galactic stellar populations and dust,
- the CCSNR measurements for galaxies with morphological type and luminosity similar to these of the MW,
- probes of CCSN explosions, such as the census of massive stars, the birth rate of NSs, the age distribution of SN remnants, the ^{26}Al distribution in the Galaxy.

These estimates are summarized in table 15.

CCSNR from historical records and Galaxy models. Historical records indicate that five SN events have occurred in the Milky Way over the past millennium: SN1006 (SNIa), SN1054 (CCSN), SN1181 (CCSN), SN1572 (SNIa) and SN1604 (SNIa). Their apparent

JCAP03(2026)081